

A Corticothalamic Circuit for Dynamic Switching between Feature Detection and Discrimination

Highlights

- Layer 6 corticothalamic neurons (L6 CTs) were activated in mouse auditory cortex
- L6 CTs enhance or suppress tuning in cortex and thalamus, depending on timing
- L6 CTs enhance behavioral sound detection or discrimination, depending on timing
- L6 CTs reset the phase of cortical delta-theta rhythms via fast-spiking neurons

Authors

Wei Guo, Amanda R. Clause,
Asa Barth-Maroon, Daniel B. Polley

Correspondence

daniel_polley@meei.harvard.edu

In Brief

Guo et al. demonstrate that layer 6 corticothalamic neurons (CT) bidirectionally modulate sound perception and auditory tuning. The time interval separating CT spiking and stimulus onset shifted modes of processing between detection at the expense of discrimination and vice versa.

A Corticothalamic Circuit for Dynamic Switching between Feature Detection and Discrimination

Wei Guo,^{1,2,4} Amanda R. Clause,¹ Asa Barth-Marón,¹ and Daniel B. Polley^{1,3,5,*}

¹Eaton-Peabody Laboratories, Massachusetts Eye and Ear Infirmary, Boston, MA 02114, USA

²Center for Computational Neuroscience and Neural Technology, Boston University, Boston, MA 02215, USA

³Department of Otolaryngology, Harvard Medical School, Boston, MA 02114, USA

⁴Present address: Picower Institute for Learning and Memory, Massachusetts Institute of Technology, Cambridge, MA 02139, USA

⁵Lead Contact

*Correspondence: daniel_polley@meei.harvard.edu

<http://dx.doi.org/10.1016/j.neuron.2017.05.019>

SUMMARY

Sensory processing must be sensitive enough to encode faint signals near the noise floor but selective enough to differentiate between similar stimuli. Here we describe a layer 6 corticothalamic (L6 CT) circuit in the mouse auditory forebrain that alternately biases sound processing toward hypersensitivity and improved behavioral sound detection or dampened excitability and enhanced sound discrimination. Optogenetic activation of L6 CT neurons could increase or decrease the gain and tuning precision in the thalamus and all layers of the cortical column, depending on the timing between L6 CT activation and sensory stimulation. The direction of neural and perceptual modulation – enhanced detection at the expense of discrimination or vice versa – arose from the interaction of L6 CT neurons and subnetworks of fast-spiking inhibitory neurons that reset the phase of low-frequency cortical rhythms. These findings suggest that L6 CT neurons contribute to the resolution of the competing demands of detection and discrimination.

INTRODUCTION

Environmental stimuli are transduced, amplified, and spatially enhanced by low-level circuits contained within the brainstem and sensory end organs. Afferent sensory traces undergo another set of transformations upon reaching forebrain sensory areas, where they are contextualized according to internal state, recent stimulus histories, long-term sensory experience, and top-down predictions of behavioral relevance (David et al., 2012; McGinley et al., 2015; Mesgarani and Chang, 2012; Polley et al., 2006; Shuler and Bear, 2006; Sohoglu and Chait, 2016). Adaptive modulation of forebrain sensory traces is accomplished through the interaction of long-range neuromodulatory inputs with local excitatory-inhibitory microcircuits (Fu et al., 2014; Kuchibhotla et al., 2017; Letzkus et al., 2011; Marlin et al., 2015; Pi et al., 2013; Pinto et al., 2013; Schneider et al.,

2014; Zhou et al., 2014). The contribution of corticothalamic (CT) neurons to forebrain sensory modulation is intriguing in this respect, as CT neurons feature both a long-range feedback projection to the thalamus and dense local connectivity with excitatory and inhibitory neurons within the cortical column (Bortone et al., 2014; Bourassa and Deschênes, 1995; Briggs et al., 2016; Llano and Sherman, 2008; Winer et al., 2001; Zhang and Deschênes, 1997; S. Ramon y Cajal, 1906 Nobel lecture).

Layer 6 (L6) CTs are glutamatergic pyramidal neurons, yet their targeted activation via optogenetic strategies primarily induces a net suppression of spontaneous and sensory-evoked activity in the cortex via direct connections onto local fast-spiking (FS) inhibitory neurons (Bortone et al., 2014; Kim et al., 2014; Olsen et al., 2012). Whereas activating L6 CT neurons scales down sensory-evoked responses in most layers of the cortical column, these neurons' effect on thalamic responses is a mixture of modest facilitation and suppression (Denman and Contreras, 2015; Mease et al., 2014; Olsen et al., 2012; Temereanca and Simons, 2004). A recent study performed in somatosensory thalamocortical slice preparation has set up a new framework for studying these circuits by showing that their mode of modulation depends entirely on timing: L6 CT neurons can dynamically mediate either synaptic suppression or enhancement, depending on the frequency and time course of their activation (Crandall et al., 2015). Here, we pursue this idea in the intact animal by showing that L6 CT neurons can impose multiple forms of modulation on auditory responses in the primary auditory cortex (A1) and medial geniculate body of the thalamus (MGB), where again the sign of modulation—suppression or enhancement—depends on the timing between sensory stimuli and L6 CT spiking.

Enhancement or suppression of cortical sensory representations has an immediate and direct impact on perceptual salience as studied behaviorally (Froemke et al., 2013; Pinto et al., 2013; Sohoglu and Chait, 2016). Studies of sensory processing in humans and non-human primates suggest that cortical networks can enhance detection, segregate stimulus sources, and suppress distracting stimuli by organizing the frequency and phase of low-frequency oscillations in the cortical electrical field (Giraud and Poeppel, 2012; Schroeder and Lakatos, 2009). A stimulus falling on the high-excitability phase of a cortical oscillation would recruit strong spiking in principal neurons and robust perception, whereas the same stimulus falling on the low excitability phase might fail to drive spiking activity and could go

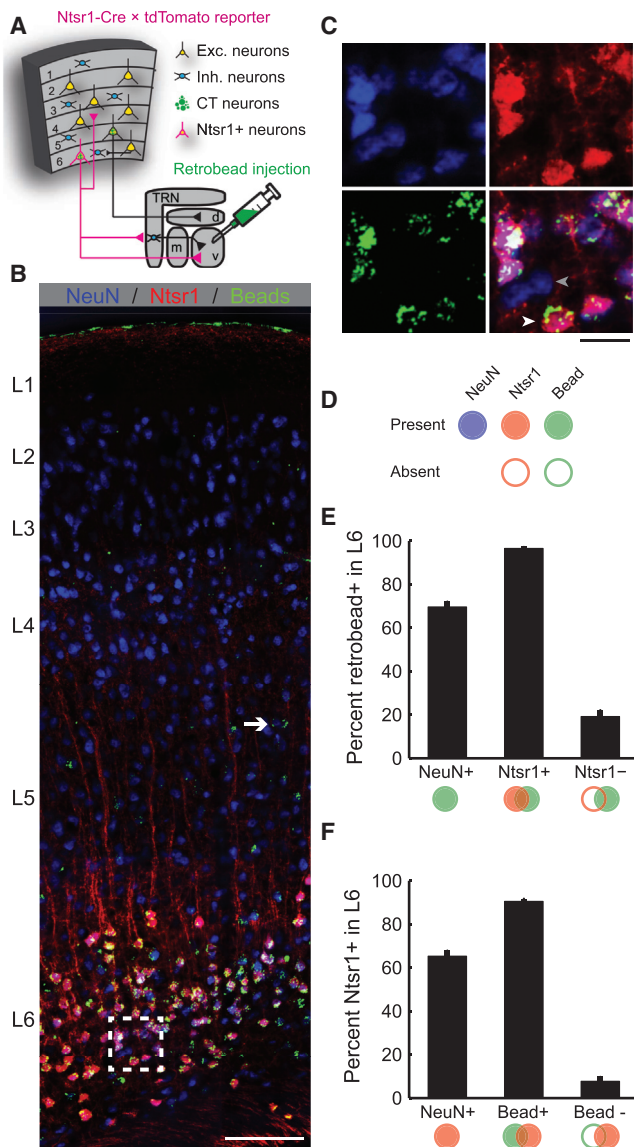


Figure 1. A Transgenic Strategy to Selectively Target Layer 6 Auditory Corticothalamic Neurons

(A) *Ntsr1-Cre* mice were crossed with a Cre-dependent tdTomato reporter line. Fluorescent microspheres injected into the medial geniculate body (MGB) were retrogradely transported to the cell bodies of CT neurons in the auditory cortex. (B) After allowing the thalamic beads 7 days for retrograde transport, coronal sections of auditory cortex were immunolabeled for NeuN, a ubiquitous neural marker. As expected, CT cell bodies identified with green beads were occasionally found in L5 (white arrow) but were concentrated in L6, where *Ntsr1+* cell bodies (red) were abundant. Scale bar, 100 μ m. (C) Magnification of area designated by white square in (B). Many L6 neurons (blue channel, top left) are *Ntsr1+* (red channel, top right) and project to a MGB region near the retrobead injection zone (green channel, bottom left). L6 neurons that do not project to the MGB and do not express *Ntsr1-Cre* (gray arrowhead, bottom right) are interspersed among *Ntsr1+* L6 CT neurons (white arrowhead). Scale bar, 10 μ m. (D) We quantified the percentage of L6 neurons that were CT and/or *Ntsr1+* in 824 L6 neurons from eight hemispheres of four mice. (E and F) Summary histograms for the percentage of neurons that were positive or negative for (E) beads or (F) *Ntsr1*. Approximately 35% of L6 neurons do

undetected (Lakatos et al., 2008; Zion Golumbic et al., 2013). A neural circuit responsible for controlling the phase of low-frequency cortical rhythms has yet to be identified.

Here, we present findings that bring these studies into alignment by showing that L6 CT neurons, in agreement with studies in the acute thalamocortical slice, can both enhance and suppress activity in the cortex and thalamus of awake mice depending on the temporal interval between their spiking and sensory-evoked responses (Crandall et al., 2015). In keeping with prior observations in visual cortex, we also find that L6 CT neurons are functionally connected with a subtype of FS interneuron that modulates sensory gain in all layers of the cortical column (Bortone et al., 2014; Olsen et al., 2012). Finally, as per recent studies in non-human primates, we show that activating and deactivating L6 CT and FS neurons generates distinct cortical rhythms that modulate the excitability of cortical sensory responses and bias perceptual processing toward modes that favor the enhanced detection of faint sounds or the enhanced resolution of similar sounds (Lakatos et al., 2008). However, unlike earlier studies, we report here that the most striking effects of L6 CT neurons on thalamocortical sound processing and auditory perception are found immediately after L6 CT neurons stop spiking; concurrent presentation of sound stimuli with L6 CT activation induces a weaker additive increase in spiking with no demonstrable effect on sound detection or discrimination.

RESULTS

Ntsr1-Cre Targets a Subset of L6 Neurons in Auditory Cortex that Project to the Thalamus

Recent studies of corticothalamic modulation have taken advantage of the *Ntsr1-Cre* transgenic mouse, which labels a subpopulation of pyramidal neurons in L6 that have both short-range vertical connections within the cortical column and subcortical projections that deposit axon collaterals in the thalamic reticular nucleus (TRN) en route to the dorsal thalamus (Bortone et al., 2014; Gong et al., 2007; Kim et al., 2014; Lee et al., 2012; Olsen et al., 2012). Anatomical tracer experiments in the visual and somatosensory cortex confirmed that virtually all *Ntsr1*-positive neurons (*Ntsr1+*) are L6 corticothalamic (L6 CT), and virtually all L6 CT neurons are *Ntsr1+* (Bortone et al., 2014; Kim et al., 2014). To determine whether the same specificity exists in the auditory cortex, we crossed the *Ntsr1-Cre* line with a Cre-dependent tdTomato reporter line and injected green fluorescent microspheres into the MGB of their double-transgenic offspring (Figure 1A). After allowing the beads 1 week for retrograde transport, we immunolabeled coronal sections of the auditory cortex for the ubiquitous neuron marker NeuN and compared the colocalization of beads in *Ntsr1+* neurons ($n = 824$ neurons from eight hemispheres of four mice, Figures 1B–1D). We observed that approximately 35% of L6 neurons neither projected to the MGB nor expressed *Ntsr1*; they were therefore most likely intracortical neurons (Figures 1E–1F, left bars). Among *Ntsr1+* neurons, 97% also contained beads, indicating that nearly all *Ntsr1+* neurons

not express *Ntsr1* and do not project to the MGB retrobead injection zone (left bars). By contrast, 97% of L6 *Ntsr1+* neurons project to the MGB, confirming that *Ntsr1-Cre* selectively targets L6 CT neurons in the auditory cortex.

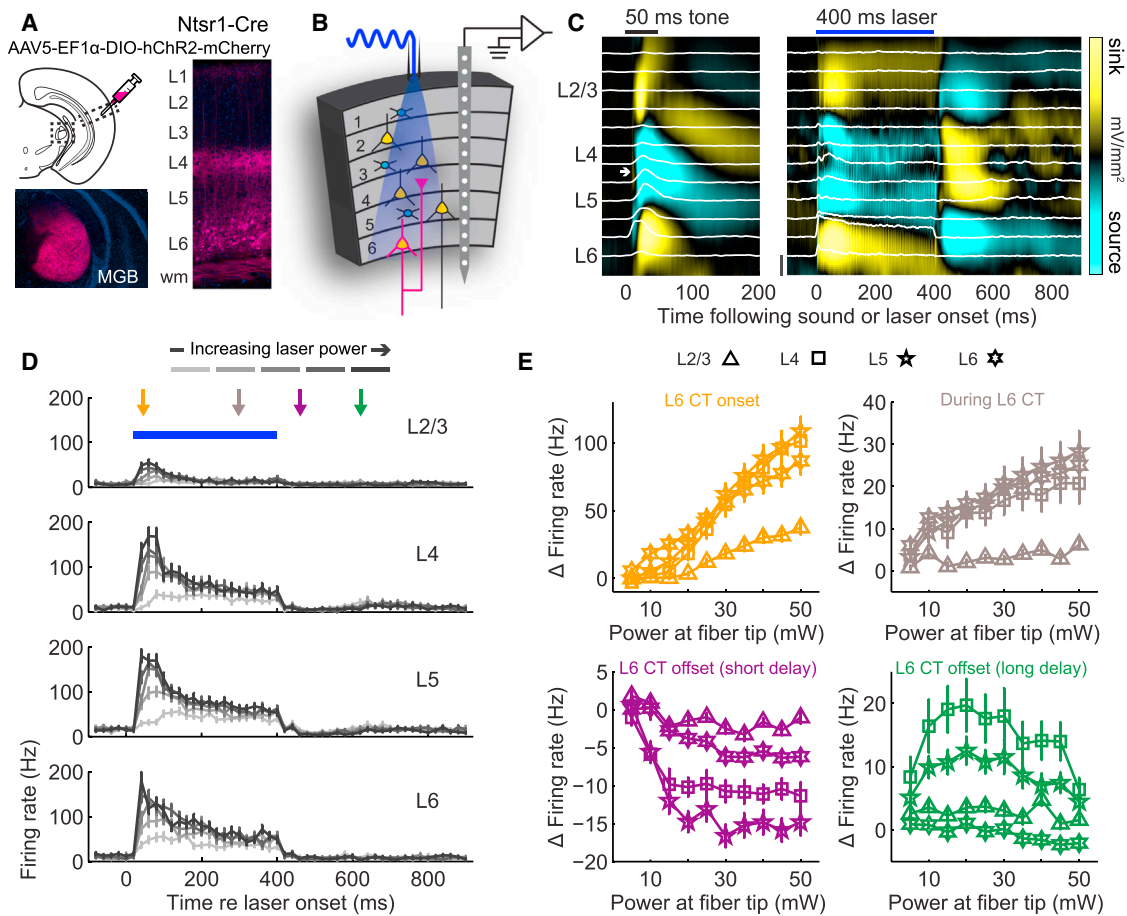


Figure 2. Optogenetic Activation of L6 CT Neurons in A1 Induces Alternating Periods of Spike Enhancement and Suppression

(A) ChR2 was expressed in L6 CT neurons by injecting a Cre-dependent viral construct into A1 of *Ntsr1-Cre* mice. The fluorescent mCherry reporter is visible in L6 cell bodies, in dense bands of neuropil in L4, and in MGB axons.

(B) Schematic of columnar recording during L6 CT activation.

(C) Sound-evoked (left) and laser-evoked (right) laminar profiles of current source density (CSD) amplitude from a single A1 penetration in an awake mouse. Multiunit activity (MUA) at each location is represented by the superimposed white peristimulus time histograms (PSTH; scale bar, 100 spikes per s). White arrow indicates a brief, early sound-evoked current sink used to identify L4.

(D) PSTHs represent the mean MUA in each layer. Laser power at the tip of the optic fiber ranges from 5 to 50 mW. Error bars represent 1 SEM.

(E) The change in laser-evoked firing rates relative to baseline activity increase monotonically during the onset and sustained periods (ANOVA, $F > 10$, $p < 1 \times 10^{-6}$ for each, orange and gray arrows, respectively), decrease immediately following laser offset ($F = 22.99$, $p < 1 \times 10^{-6}$, purple arrow) and increase again 100 ms later ($F = 4.01$, $p < 5 \times 10^{-5}$, green arrow), particularly in L2/3, L4, and L5. Error bars represent 1 SEM. A detailed breakdown of all statistical tests can be found in [Table S1](#).

are CT. This is remarkable, considering that the not all CT neurons would necessarily be expected to innervate the region of the lateral MGB targeted for retrobead injection (Figure 1E). Conversely, 90% of L6 CT neurons were also *Ntsr1+* (Figure 1F). Therefore, while a small fraction of L6 CT neurons may not express *Ntsr1-Cre*, virtually all *Ntsr1+* neurons in the auditory cortex are in L6 and are CT, confirming prior reports made in the visual and somatosensory cortex that the *Ntsr1-Cre* line offers a powerful approach to the study of L6 CT projection neurons.

L6 CT Neurons Induce Alternating Periods of Activation and Suppression across the Cortical Column

To manipulate the activity of L6 CT neurons, we expressed channelrhodopsin (ChR2) in the auditory cortex of adult *Ntsr1-Cre*

mice using a Cre-dependent viral construct. *Ntsr1+* soma were observed in L6 with intense neuropil staining in L4 of A1 and the ipsilateral MGB and a fainter band of labeling in L1 (Figure 2A). We recorded unit activity from all layers of the primary auditory cortex (A1) in awake, head-fixed mice while activating L6 CT neurons with blue light ($n = 418$ recording sites from 11 mice; Figures 2B and 2C). Whereas optogenetic activation of L6 CT neurons suppresses spiking in V1 (Olsen et al., 2012), it increases firing rates in all layers of A1 (Figure 2D; refer to Table S1 and figure legends for all statistical reporting). Closer inspection revealed that firing rate elevation was observed at the onset and steady state of laser activation, yet robust suppression of spiking was observed at a short delay following the offset of laser activation (50–100 ms after laser offset) and followed by rebound

excitation at a longer delay after laser offset (150–200 ms after laser offset) (Figure 2E). Thus, the effect of optogenetically activating L6 CT neurons in A1 was opposite to prior reports in V1. Moreover, deactivation of L6 CT neurons upon laser offset initiated an alternating pattern of spiking suppression and facilitation that has not been described previously. None of these phenomena were observed in *Ntsr1-Cre* mice injected with a reporter virus that did not encode Chr2 (Figure S1).

Optogenetic Activation of L6 CT Neurons Bidirectionally Modulates Sound Processing in A1

As a next step, we characterized how dynamic changes in columnar excitability elicited by L6 CT activation affected sound-evoked responses and frequency tuning. We measured pure tone frequency tuning from A1 units with or without optogenetic activation of L6 CT units (Figure 3A). Because optogenetic activation of L6 CTs induced alternating periods of enhancement and suppression, we staggered the onset of pure tone stimuli relative to laser onset at 17 discrete intervals (0–800 ms in 50 ms steps; Figure 3B). As illustrated from a representative L4 unit recording, L6 CT activation induced clear modulation of both auditory responsiveness and auditory tuning (Figure 3C). The modulation was divergent, alternating between enhancement during L6 CT activation, suppression immediately following the deactivation of L6 CT neurons, and then a second enhancement at longer delays following laser offset.

Sensory response modulation can be expressed as a linear transformation from responses without laser (r_{off}) to responses with laser (r_{on}) by the formula $r_{on} = a \times r_{off} + b$, where additive or subtractive modulation ($b > 0$ or $b < 0$, respectively) reflect constant shifts across the entire tuning function and multiplicative or divisive gain ($a > 1$, $a < 1$, respectively) reflects scaling changes that preserve the shape of the tuning function (Seybold et al., 2015). In V1, L6 CT activation induces a purely divisive scaling change, such that visual responses were suppressed without affecting orientation tuning (Olsen et al., 2012). Referring to the same representative L4 unit shown in Figure 3C, we observed a purely additive shift during L6 CT activation, divisive gain when tones were presented at a short delay following laser offset, and a multiplicative gain when tones were presented at a longer delay after laser offset (Figure 3D). By contrast, a representative L6 unit was strongly activated by the laser (likely because it expressed Chr2) but did not show any notable changes in auditory responsiveness after laser offset (Figure 3E). These effects were summarized by plotting the mean additive or subtractive and multiplicative or divisive modulation in Cartesian coordinates where pure shifting changes fell on the x axis, pure scaling changes fell along the y axis, and mixtures of shifting and scaling modulation fell on the diagonals. For units in L6, the effect of L6 CT activation was straightforward and matched prior reports in V1: the evoked-firing rate change was purely additive during laser with comparatively modest modulation at later time periods. For units in L2/3–L5, L6 CT activation induced a tripartite modulation of auditory responses: additive scaling during L6 CT activation, divisive gain shortly after L6 CT deactivation (50 ms following laser offset), and multiplicative gain at a longer delay following L6 CT deactivation (150 ms following laser offset) (Figure 3F).

One possibility is that these dynamics arose from an unrealistically long and intense period of L6 CT activation. We controlled for this by performing the same measurements with a shorter laser pulse set to a minimally effective amplitude (50 ms, 5 mW above threshold). The results of this stimulation paradigm were largely the same (Figure 3G). As a negative control for non-specific effects of laser activation on A1 receptive fields, we did not observe any systematic modulation of auditory responses in *Ntsr1-Cre* mice that expressed only a control fluorophore in L6 CT units ($n = 96$ recording sites from three mice; Figure 3G, inset). Importantly, the modulation of tone-evoked responses after laser offset was not purely divisive or multiplicative. The significant subtractive and additive components observed in the short- and long-delay modulation, respectively, suggested that the precision of frequency tuning was also affected. Indeed, for several cortical layers, frequency tuning was significantly narrower during the short delay period and significantly wider during the long delay period following laser offset (Figure 3H).

Optogenetic Activation of L6 CT Neurons Can Alternately Bias Sound Perception toward Enhanced Detection or Discrimination

To study L6 CT modulation of sound perception, we implanted optic fibers over the left and right auditory cortex of *Ntsr1-Cre* mice that expressed Chr2 in A1 of both hemispheres and measured their sound detection and discrimination performance in an auditory avoidance task ($n = 5$ mice). In this task, mice were trained to cross from one side of a shuttlebox to the other shortly following the presentation of tone pips at the target frequency, but not to foil tones at other frequencies (Figure 4A). The distinct forms of receptive field modulation during L6 CT activation or shortly following L6 CT deactivation inspired two hypotheses (Figure 4B, left): 1) The divisive or subtractive gain observed at a short delay following laser offset (50 ms) would suppress A1 activity, thereby impairing tone detection; however, the sharper tuning would improve frequency discrimination. 2) Conversely, the multiplicative or additive gain observed at the longer delay period following laser offset (150 ms) would enhance tone-evoked activity and improve tone detection performance; however, the loss of tuning precision would impair tone discrimination.

We tested these predictions by interleaving behavioral trials where 50 ms tone pips were presented 1) without L6 CT activation (tone alone), 2) concurrent with 50 ms pulses of L6 CT activation, 3) shortly after L6 CT deactivation, or 4) at a longer delay following L6 CT deactivation (Figure 4B, right). Importantly, activating L6 CT neurons without tone presentation did not cause mice to “hear the light” and cross sides of the shuttle box, as described previously with non-specific optogenetic activation of subcortical auditory centers (Guo et al., 2015) (Figure 4C, left). Mice performed predictably on tone-alone trials; the likelihood of detecting the target tone increased with sound level, and false alarms with these easily discriminable frequencies were rare (Figure 4C, black). Concurrent L6 CT activation did not affect tone detection performance (Figure 4C, orange). Compared to tone-alone trials, target detection was impaired in short-delay trials but significantly enhanced in long-delay trials—without any non-specific effects on foil tones (Figure 4C, purple and green).

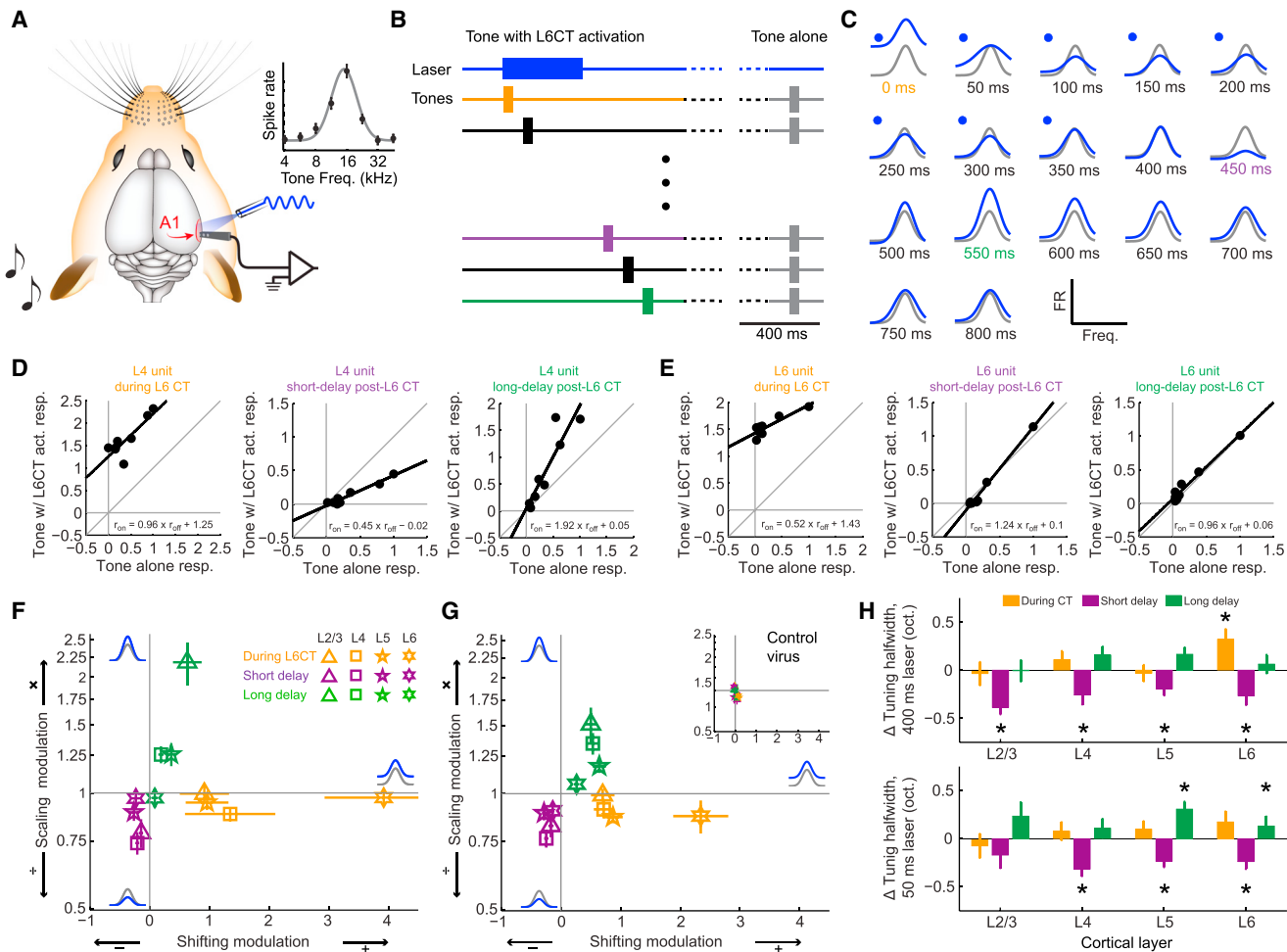


Figure 3. Activating L6 CT Neurons Induces a Triphasic Modulation of Sound-Evoked A1 Responses

(A) Pure tone pips were presented to the left ear while recording spiking activity from the contralateral A1 with and without optogenetic activation of L6 CT neurons. Frequency response functions are illustrated with a Gaussian fit.

(B) Tones were presented without L6 CT activation (50% of trials, gray) or with L6 CT activation; the delay between the onset of tone bursts and laser pulses varied from 0–800 ms.

(C) L6 CT activation imposed diverse forms of modulation on a representative L4 recording site.

(D and E) The scaling and shifting components were computed in the same example L4 site (D) and a representative L6 site (E) by regressing the mean normalized, tone-evoked firing rates measured during the tone-alone trials against the firing rates recorded during the three epochs surrounding L6 CT activation.

(F and G) Mean (\pm SEM) shifting and scaling modulations were computed for each multiunit site for recordings made with a 400 ms laser pulse at 20 mW (F) or a 50 ms laser pulse set to a minimally effective laser power (G). Inset: Laser-induced tuning modulation was not observed from a separate cohort of mice injected with a control virus (Mixed-design ANOVA, main effect for shifting modulation: $F[2,20] = 0.24$, $p = 0.79$; main effect for scaling modulation: $F[2,20] = 2.17$, $p = 0.14$). Statistically significant shifting and scaling modulation for all permutations of laser duration, response period, and layer were determined with one-sample t tests against a population mean of 0 (shifting modulation) or 1.0 (scaling modulation). Looking across both laser durations, we observed significant additive changes during L6 CT activation in L2/3, L5, and L6 ($p < 0.05$ for each) and significant divisive gain in L4 and L5 ($p < 0.05$ for each). In the short delay period following L6 CT deactivation, we observed significant subtractive changes in all layers and significant divisive gain in all but L6 ($p < 0.005$ for each). In the long delay period following L6 CT deactivation, we observed significant additive and multiplicative changes for L2/3, L4, and L5 ($p < 0.05$ for each) but no significant change in L6 tuning ($p > 0.1$ for each).

(H) The mixture of shifting and scaling modulation created sharper frequency tuning during the short delay period but wider frequency tuning in the long delay period. Tuning changes in octaves (oct.) are estimated from the change in width at half-height between the tone-alone and tone-and-L6-CT activation for the 400 ms laser (top) and 50 ms laser (bottom) conditions. Asterisks indicate $p < 0.05$ with a one-sample t test relative to a population mean of 0.

We observed the opposite pattern of perceptual changes when mice were required to discriminate between increasingly similar tone frequencies rather than to detect faint tones. In the tone-alone condition, mice were unable to discriminate the target and foil frequencies when they differed by 10% or less

(Figure 4D, black). Concurrent L6 CT activation had no effect on tone discrimination (Figure 4D, orange). In the short delay period, where divisive or subtractive modulation dominated A1 responses, accurate discrimination of targets and foils persisted at frequency differences as small as 10%, even though detection

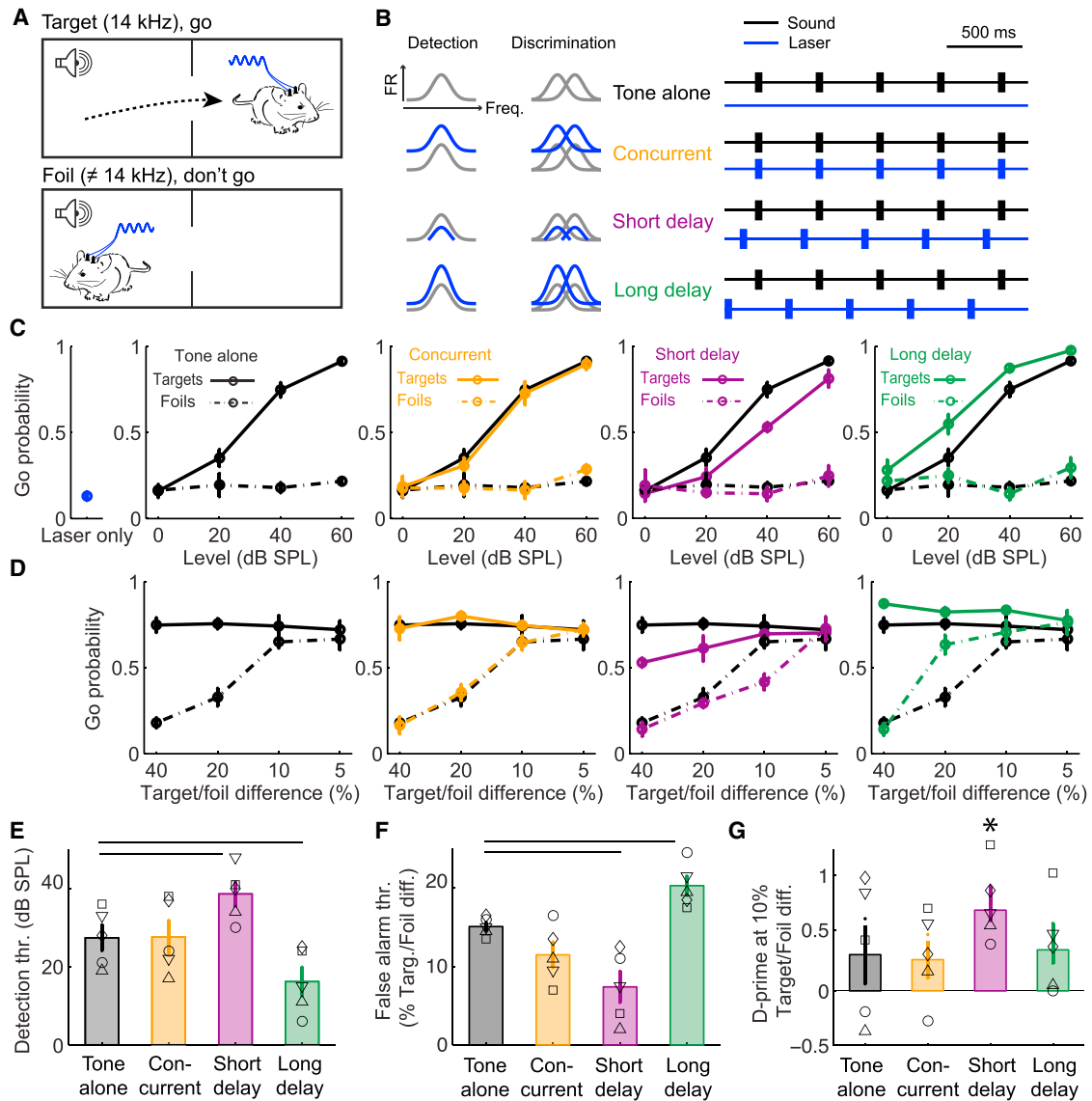


Figure 4. L6 CT Activation Can Bias Sound Perception toward Enhanced Detection at the Expense of Discrimination or Vice Versa

(A) Mice were trained in an auditory avoidance task that required them to cross from one side of a shuttle box to the other shortly following the presentation of 14 kHz tone bursts (target) but not tones of other frequencies (foils). Mice expressed ChR2 in L6 CT neurons in left and right auditory cortex and were implanted with bilateral optic fiber assemblies.

(B) Schematic of A1 tuning modulation and design of behavioral optogenetics experiment. The distinct types of receptive field modulation following L6 CT deactivation were predicted to have dissociable effects on tone detection and discrimination behaviors.

(C) Probability of a “Go” (i.e., crossing) response for target tones, foil tones, the laser stimulus alone, and the three combined tone and laser test conditions as a function of sound level. Compared to tone-alone trials, target detection is impaired in the short-delay configuration but enhanced in the long-delay configuration (ANOVA, main effects for delay, $F = 10.44$, $p < 0.005$ for short and long conditions).

(D) Probability of a Go response as a function of frequency separation between the target tone and the foil tone at a fixed sound level (40 dB SPL). Discrimination is enhanced for difficult conditions (10%) in the short-delay condition but is reduced in easy conditions (20%) in the long-delay condition (ANOVA, main effect for delay condition, $F = 14.3$, $p < 0.0005$ for both short and long delays).

(E) Mean (± 1 SEM) target detection threshold (thr.), defined as the sound level associated with a 50% probability of making a Go response on target trials.

(F) Mean (± 1 SEM) false alarm threshold, defined as the frequency spacing associated with a 50% probability of making a Go response on foil trials. Horizontal lines in (E) and (F) represent $p < 0.05$ using a paired t test between tone-alone and the corresponding tone + laser condition, after correcting for multiple comparisons.

(G) Overall sensitivity, as measured with the d' statistic, was higher on short-delay trials, but the difference is not statistically significant after correcting for multiple comparisons (paired t test, $p = 0.16$). However, the d' statistic was significantly different than zero (no separation between the hit and false positive distributions) for the short delay period, indicated by asterisk (one-sample t test, $p < 0.001$, $p > 0.1$ for all other conditions).

was impaired overall (Figure 4D, purple). In the long delay period, where multiplicative or additive modulation was prevalent, discrimination was impaired for targets and foils that were separated by as much as 20%, even though detection of target tones was enhanced overall (Figure 4D, green).

These findings demonstrate that L6 CT neurons can enhance sensory feature detection or discrimination depending on the relative timing between their activation and sensory stimuli. Compared to tone-alone trials, detection thresholds were elevated by 11.2 ± 1.9 dB when tones were presented 50 ms after L6 CT neurons were deactivated, but were improved by 11.4 ± 2.6 dB on trials where the delay was just 100 ms longer (Figure 4E). On the other hand, the threshold for mistaking the foil tone frequency for the target frequency (false alarm) was reduced to a $8.7\% \pm 1.17\%$ difference at the short delay following L6 CT deactivation but was increased to $20.7\% \pm 1.87\%$ on long-delay trials (Figure 4F). Discriminability of similar tones (10% between target and foil), estimated here with the d' statistic, was only significantly different than zero during the short delay period when A1 responses were suppressed and tuning was more precise (Figure 4G). Thus, the perceptual effects of L6 CT activation were robust (net effect on tone detectability and discriminability > 20 dB and $> 25\%$, respectively), were only observed in trials where L6 CT activation preceded sound onset, and were bidirectional, supporting either feature detection or feature discrimination.

L6 CT Neurons Enhance A1 Sound Responses by Modulating a Thalamic Microcircuit

In addition to their local connections within A1, L6 CT neurons deposit axon collaterals in the thalamic reticular nucleus (TRN) before terminating in the ventral subdivision of the medial geniculate body of the thalamus (MGBv, Figure 5A). The auditory subregion of TRN is composed of GABAergic neurons that project to MGBv, whereas the mouse MGBv contains no GABAergic interneurons, but rather only glutamatergic neurons that project both to TRN and to the middle layers of A1 (Hackett et al., 2016; Ito et al., 2011; Jones, 2007; Figure 5B). Modulation of A1 responses could arise either through local circuit effects of L6 CT neurons within the cortical column or could be inherited from the dynamic interplay of inhibition and excitation between TRN and MGBv. To characterize whether and how receptive field modulation in A1 could be attributed to changes at the level of the thalamus, we recorded from all layers of the A1 column in head-fixed, awake mice during L6 CT activation while making simultaneous recordings from tonotopically matched regions of the MGBv ($n = 106$ recordings sites from five mice) or TRN ($n = 24$ recording sites from two mice, Figure 5C).

We found that auditory responses were enhanced in both MGB and TRN during L6 CT activation (50ms), much as they were in A1 (Figures 5D–5F, orange). Shortly following the offset of L6 CT activation, when A1 responses were strongly suppressed, frequency tuning in MGBv and TRN was not significantly changed from the tone-alone condition (Figures 5D–5F, purple). During the long delay period following laser offset, frequency tuning in MGBv showed a comparable level of multiplicative or additive enhancement as was simultaneously observed in A1 (Figures 5D–5F, green). Interestingly, we found that TRN

modulation during the long delay period was inverted; whereas MGB and A1 both showed multiplicative or additive modulation 150 ms after laser offset, tuning modulation in the TRN was a mixture of divisive and subtractive.

These findings led us to conclude that enhanced behavioral detection and A1 unit responses at the longer delay following L6 CT deactivation could be fully explained by a change in sound-evoked MGBv activity. Whereas MGBv and A1 unit responses were enhanced at a longer delay following L6 CT deactivation, the modulation of sound-evoked activity in TRN was matched in strength but was opposite in sign. This suggests that enhanced auditory responsiveness at longer delays following L6 CT deactivation could have arisen from a purely intra-thalamic circuit wherein the feedforward inhibition from TRN to MGBv is scaled down over time, as has been suggested from studies of L6 CT activation in thalamocortical slice recordings (Crandall et al., 2015). Reduced inhibition from TRN could disinhibit MGBv neurons, making them hypersensitive to auditory stimulation (Sherman and Guillery, 2002). By contrast, there was no thalamic antecedent for the robust A1 suppression observed just after L6 CT neurons were deactivated. This raises the possibility that enhanced frequency discrimination, reduced tone detection and suppressed A1 responses observed shortly following L6 CT deactivation were not mediated by the L6 feedback to the thalamus, but instead were mediated through the intracortical connections of L6 CT neurons.

L6 CT Activation Changes the Frequency and Resets the Phase of Low-Frequency Cortical Rhythms

Cortical spiking activity rides on a background of slower undulations in the underlying electric field (Figures S2A–S2C). The cortical local field potential is generated by the flow of transmembrane currents distributed across a volume of tissue spanning hundreds of microns laterally and up to several millimeters vertically (Figure S2D) (Kajikawa and Schroeder, 2011). Low-frequency oscillations in cortical electric fields can be studied at higher spatial resolution by measuring the second spatial derivative of the local field potential, the current source density (CSD), using linear multielectrode arrays that evenly sample cortical activity across all layers (Figure S2E; Kaur et al., 2005; Müller-Preuss and Mitzdorf, 1984; Kajikawa and Schroeder, 2011). The amplitude, frequency, and phase of the underlying CSD are closely linked with spike probability and sensory tuning in auditory cortex (Figure S2F) (Kayser et al., 2015; O'Connell et al., 2011). This led us to question whether the unexplained suppression of spiking activity associated with L6 CT deactivation was linked to stereotyped changes in the underlying cortical electric field, as estimated from the translaminar CSD.

L6 CT activation induced an alternating pattern of current sinks and sources similar to the laminar signature of sound-evoked CSD signals (Figure 2C). When studied in the time domain, L6 CT activation drove robust, high-frequency oscillations across the cortical column (Figure 6A) with a distinct high gamma peak in L5 and L6 (110 Hz with its 220 Hz harmonic) and two peaks in the high gamma range in L2/3 and L4 (40 Hz and 110 Hz) (Figure 6B). By contrast, L6 CT activation in V1 elicits a single peak in the L6 frequency spectrum at 60 Hz (Olsen et al., 2012). Abrupt cessation of L6 CT spiking at laser offset initiated a low-frequency

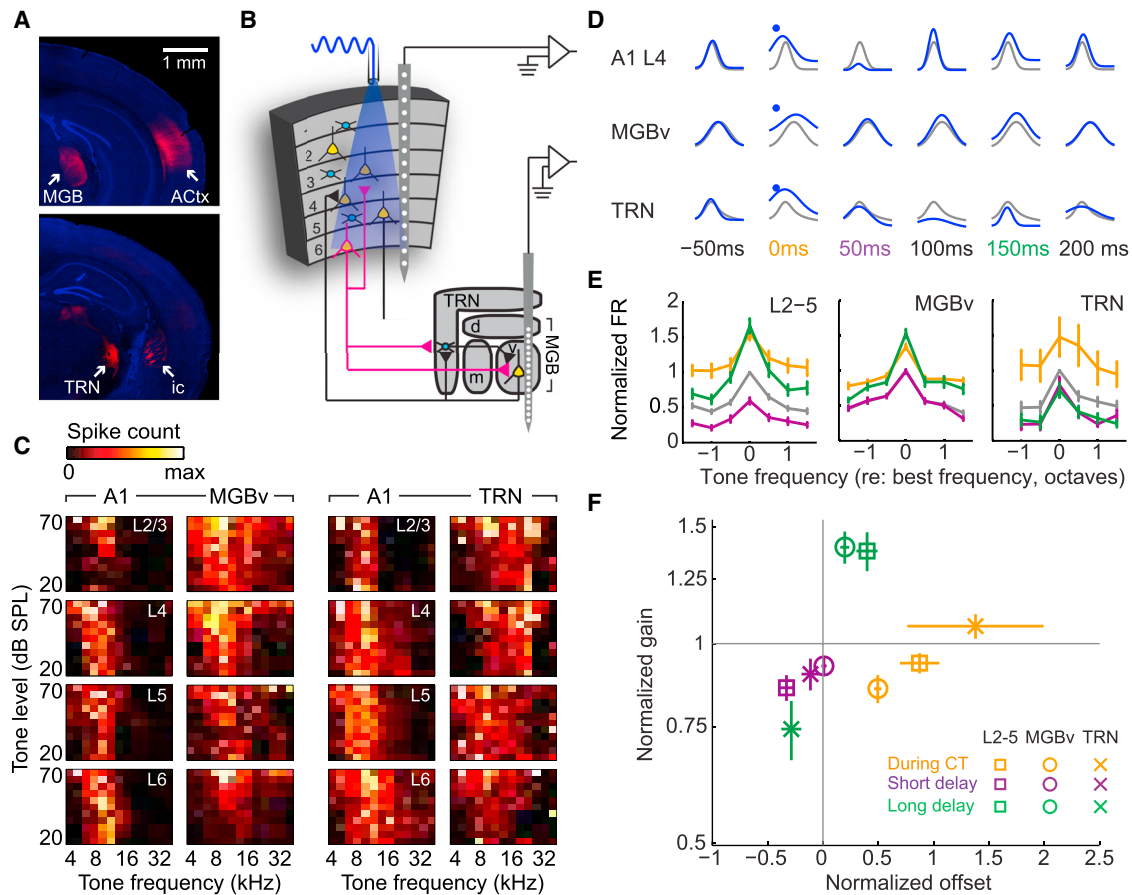


Figure 5. Enhanced A1 Responses at Long Delays following L6 CT Activation Can Be Attributed to Short-Term Dynamics in Thalamic Sound Processing

(A) Coronal sections showing mCherry expression in auditory L6 CT neurons and medial geniculate body (MGB) axon terminals (top) as well as a more rostral section showing the L6 CT axon bundle in the internal capsule (ic) and collaterals in the thalamic reticular nucleus (TRN, bottom).

(B) Schematic of procedure for simultaneous recordings of the A1 column and either MGB or TRN in awake, head-fixed mice. The ventral, medial, and dorsal subdivisions of the MGB are illustrated (v, m, and d, respectively). Parameters for L6 CT activation laser were a 50 ms duration laser pulse 5 mW above threshold.

(C) Frequency response areas (FRAs) from simultaneously recorded A1/MGB or A1/TRN sites. Recordings were topographically aligned such that frequency tuning was roughly matched between cortical and thalamic sites.

(D) Iso-intensity frequency tuning functions from representative L4, MGB, and TRN recording sites. The gray and blue functions correspond to the tone-alone and tone-and-laser conditions, respectively. Enhanced auditory responses are observed in both A1 and thalamus when tones and L6 CT activation are concurrent (orange). Divisive suppression is found in A1 shortly after L6 CT deactivation, but not in either thalamic recording site (purple). Multiplicative enhancement is observed at this interval.

(E) Mean (± 1 SEM) tone-evoked firing rates normalized to the best frequency in the tone-alone condition (gray). Compared to tone-alone responses, firing rates were significantly elevated with concurrent L6 CT activation in A1, MGB, and TRN units (paired t test, $p < 0.05$); during the short delay period, A1 and TRN units showed significantly reduced firing rates (paired t test, $p < 0.05$), while MGB units showed unchanged firing rates ($p > 0.05$); during the long delay period, A1 and MGB units showed significantly enhanced firing rates ($p < 0.05$), while TRN units showed significantly reduced firing rates ($p < 0.05$).

(F) Mean (± 1 SEM) shifting and scaling modulation computed for each multiunit site with the paired recording approach. Statistically significant shifting and scaling modulations for all permutations of laser duration, response period, and brain structure were determined with one-sample t tests against a population mean of 0 (shifting modulation) or 1.0 (scaling modulation). We observed significant additive gain during L6 CT activation in L2–L5 and MGB and significant divisive gain in L2–L5 ($p < 0.05$ for each). In the short delay period following L6 CT deactivation, we observed significant subtractive and divisive gain only in L2–L5 ($p < 0.05$ for both). In the long delay period following L6 CT deactivation, we observed significant additive gain in MGB and L2–L5, significant multiplicative gain in L2–L5 and MGB, and significant subtractive and divisive gain in TRN ($p < 0.05$ for each).

delta-theta rhythm (2–6 Hz) across all layers (Figure 6C). L6 CT deactivation induced one reliable cycle of this delta-theta rhythm regardless of laser duration, with a L2/3 current source occurring 50–100 ms after laser offset and a current sink occurring 100–200 ms later (Figure 6D). Prior work demonstrates a strong correlation between spike probability and the phase of the L2/3 low-

frequency cortical phase, with low spiking probability associated with the upstroke of the current source (at 0 radians) and high spiking probability aligned to the downstroke of the current sink (π radians) (Lakatos et al., 2008, 2013). We noted that auditory suppression in the short delay period following L6 CT deactivation was aligned with the upstroke of the CSD, whereas the

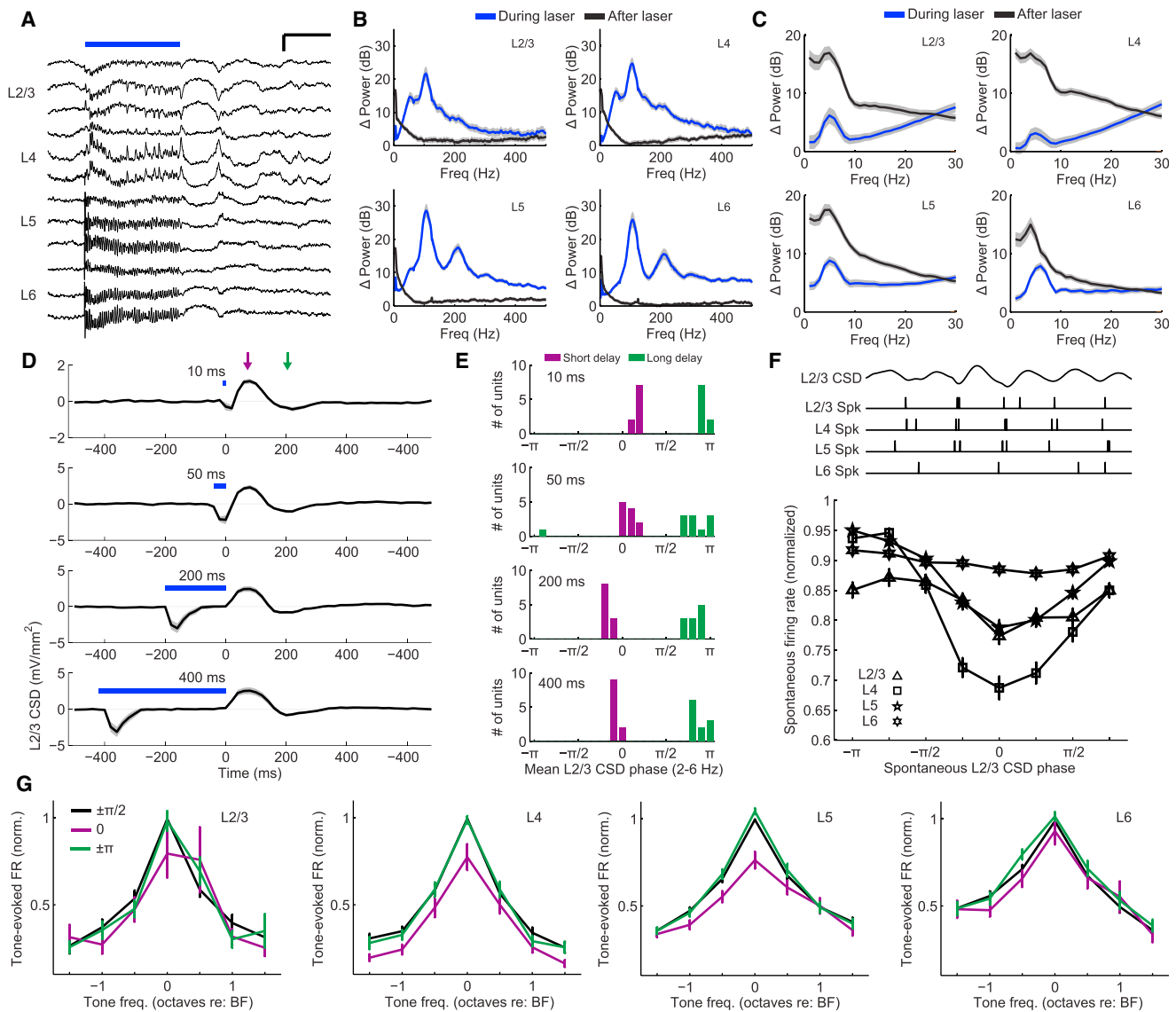


Figure 6. L6 CT Activation Changes the Frequency and Resets the Phase of Local Electric Field Oscillations in A1

(A) The raw L6-CT-evoked CSD signal recorded across the A1 column from a single trial in an awake mouse. Optogenetic activation of L6 CT neurons induces a high-frequency oscillation while the laser is on, followed by a few cycles of a low-frequency rhythm following L6 CT deactivation. Scale bar, 0.2 s and 5 mV/mm². (B and C) Change in CSD frequency power spectrum during laser (blue) and 0–400 ms after the laser is turned off (black) relative to pre-laser baseline. (B) plots the full frequency range to highlight the high-gamma peak during laser activation, whereas (C) plots frequencies ≤ 30 Hz to emphasize the delta-theta power after laser offset. (D) Mean (± 1 SEM) L2/3 unfiltered CSD amplitude for laser durations varying from 10–400 ms. The short and long delay periods following L6 CT deactivation are indicated by the purple and green arrows, respectively. (E) Phase histograms at the corresponding laser duration for the short and long delay periods. L2/3 CSD phase is consistently near zero in the short delay period and π in the long delay period. (F) Normalized spontaneous firing rate in each layer as a function of the spontaneous L2/3 delta-theta CSD phase (2–6 Hz). Spontaneous firing rate was modulated across L2/3 CSD phase for all layers (ANOVA, $F > 3.6$ and $p < 0.001$), with the lowest spike rate consistently occurring at the zero phase. (G) Tone-evoked frequency tuning functions at three phases of the spontaneously occurring L2/3 delta-theta CSD: zero, π , and the average of the intermediate phases, $\pm \pi/2$. Tuning shape was significantly modulated by phase in L4, L5, and L6 (ANOVA, $F > 6.3$, $p < 0.005$ for all), but not in L2/3 itself ($F = 1.4$, $p = 0.28$).

auditory enhancement observed in the long delay period was aligned with the CSD downstroke (Figure 6E). Importantly, the particular signature of L6 CT activation (Figure S3A), was not observed upon optogenetic activation of L5 corticofugal projec-

tion neurons (Figure S3B), cholinergic modulatory afferents from the basal forebrain (Figure S3C), parvalbumin-expressing FS interneurons (Figure S3D), or sensory activation with sound alone (Figure S3E). Therefore, the signature of strong high gamma

activity followed by a low-frequency rhythm at laser offset was specific to L6 CT neurons and is not simply the product of driving a hypersynchronous response from any population of auditory cortex neurons.

We also asked whether inactivating L6 CT units with a hyperpolarizing opsin would have effects opposite to those described with ChR2. We addressed this question by expressing the neural silencer ArchT in L6 CT units and performing an additional set of paired recordings from A1 and MGBv of awake mice ($n = 265$ units in four mice). Whereas activating L6 CT neurons that express ChR2 increased firing rates throughout the column (Figures 2 and S4A, orange data points), silencing L6 CT neurons suppresses spiking throughout the column (Figures S4B–S4D, orange data points). Similarly, while frequency tuning in A1 is strongly suppressed at a short delay following the offset of ChR2 activation (Figures 3 and 5E, purple data points), sound-evoked responses at the same delay following the offset of ArchT inactivation were enhanced (Figure S4E, purple data points). Finally, whereas activating L6CT neurons with ChR2 induces a robust high gamma rhythm (Figure 6B) followed by several cycles of delta-theta at laser offset (Figures 6B and 6C), silencing L6CT neurons only induces the low-frequency rhythm (Figure S4F). Generally, the effects of briefly inhibiting L6 CT neurons with ArchT were less pronounced than driving spiking with ChR2, and the receptive field modulation was not the exact mathematical inverse at each time interval. However, the effects of adding and removing spikes in single neurons would not be expected to have exactly symmetric effects at the level of non-linear, recurrently interconnected networks like a cortical column (Phillips and Hasenstaub, 2016; Seybold et al., 2015). As a first approximation, the effects of activating and then deactivating L6 CT neurons with ChR2 were opposite to the effects of silencing and then reactivating L6 CT neurons with ArchT.

As a final proof that the findings described here were not a purely artificial byproduct of introducing a hyper-synchronized volley of spikes with ChR2, we also characterized A1 spiking modulation when delta-theta rhythms occurred spontaneously and independent of any optogenetic activation. We found that spontaneous spike probability in A1 could be modulated by as much as 30% according to the phase of naturally occurring L2/3 delta-theta rhythms (Figure 6F). Spiking was modulated in all layers, though least in L6. As predicted, spike probability was strongly suppressed at the upstroke of the CSD (phase 0), which corresponds to the CSD phase during the short delay period following laser offset (Figure 6E). Spontaneously arising delta-theta rhythms modulated sensory tuning as well. Tone-evoked spikes falling on the zero phase of delta-theta rhythms were suppressed, leading to divisive gain of A1 tuning functions in L2/3, L4, and L5 that closely resembled the tuning modulation observed at the short delay following L6 CT deactivation (compare Figure 5E, purple, to Figure 6G, purple). Importantly, neither spontaneous spiking nor frequency tuning was enhanced at the downstroke of the CSD (phase π) relative to intermediate phases ($\pm\pi/2$). This agrees with our prior assertion that the facilitated spiking at the longer delay following L6 CT deactivation was not generated by an intracortical circuit but instead arose from dynamic switching of inhibition and excitation between MGB and TRN. By contrast, the circuit dynamics underlying

the suppressive effects of L6 CT activation were likely to arise from within A1, as has previously been described in V1 (Bortone et al., 2014). Our findings suggest that the suppressed unit responses and enhanced tone discrimination observed during the short delay period following L6 CT deactivation could be achieved by inducing a low-frequency rhythm in A1 with the low-excitability phase aligned to sensory-evoked thalamocortical inputs.

L6 CT Neurons Control Low-Frequency Network Oscillations by Driving a Subpopulation of Fast-Spiking Cortical Neurons

The preceding analysis of phase-associated spiking underscored the correlation between L6 CT-evoked delta-theta rhythms, spike probability, and sound-evoked responsiveness. As a next step, we undertook an analysis of spike-triggered changes in CSD phase and amplitude to identify a possible neural circuit that could reset the delta-theta rhythm. We examined the average cortical CSD amplitudes associated with spontaneously occurring spikes from 739 isolated single units in A1, MGB, and TRN (Figure 7A). For many single units, the spike-triggered CSD was essentially flat, suggesting that their spiking did not demonstrably change the spatiotemporal patterning of sinks and sources throughout the column. We refer to these units as “non-resetters” (Figure 7B). For other units, spontaneously occurring spikes were associated with the emergence of a clear, laminar CSD pattern. For these “resetter” units, spontaneously occurring spikes evoked one cycle of a delta-theta rhythm with a clearly defined laminar pattern of sinks and sources (Figures 6C and 7B). We rank-ordered the change in pre- versus post-spike vector strength to identify 184 single units that were clearly associated with a L2/3 CSD phase reset (Figure 7D). Variability in the free-running, spontaneous L2/3 oscillations was reset to a single phase following a resetter spike, such that the short delay period fell on the 0 phase (low excitability) and remained sharply aligned for approximately one cycle (Figure 7E).

To learn more about the properties of resetter neurons, we analyzed their occurrence as a function of spatial position (TRN, MGB, or A1 layer) and spike type (FS units, regular spiking units, or directly “phototagged” L6 CT units, Figure S2C). We found that resetter neurons could have either the FS waveform characteristically associated with parvalbumin-containing interneurons or regular-spiking waveforms (Figures 7F and S2C). They could be found in any layer of the cortical column or in MGB. There were only two conditions that failed to reveal resetter neurons: they were never found in TRN, and they were never the L6 CT neurons themselves. To distinguish between resetter neurons that might have caused CSD resets versus resetter neurons whose spikes were merely folded into an ongoing reset event, we examined the relationship between the timing of resetter neuron spikes and the onset of the CSD reset. This analysis revealed two subpopulations of resetter neurons with spike timing that significantly led—rather than lagged—resets in the spontaneous L2/3 CSD rhythm: resetter units in the ventral subdivision of the MGB (MGBvr) and cortical fast-spiking resetter units (CtxFSr) (Figure 7G).

With CSD resetter neurons functionally defined, we returned to the question of how L6 CT units reset the phase of the

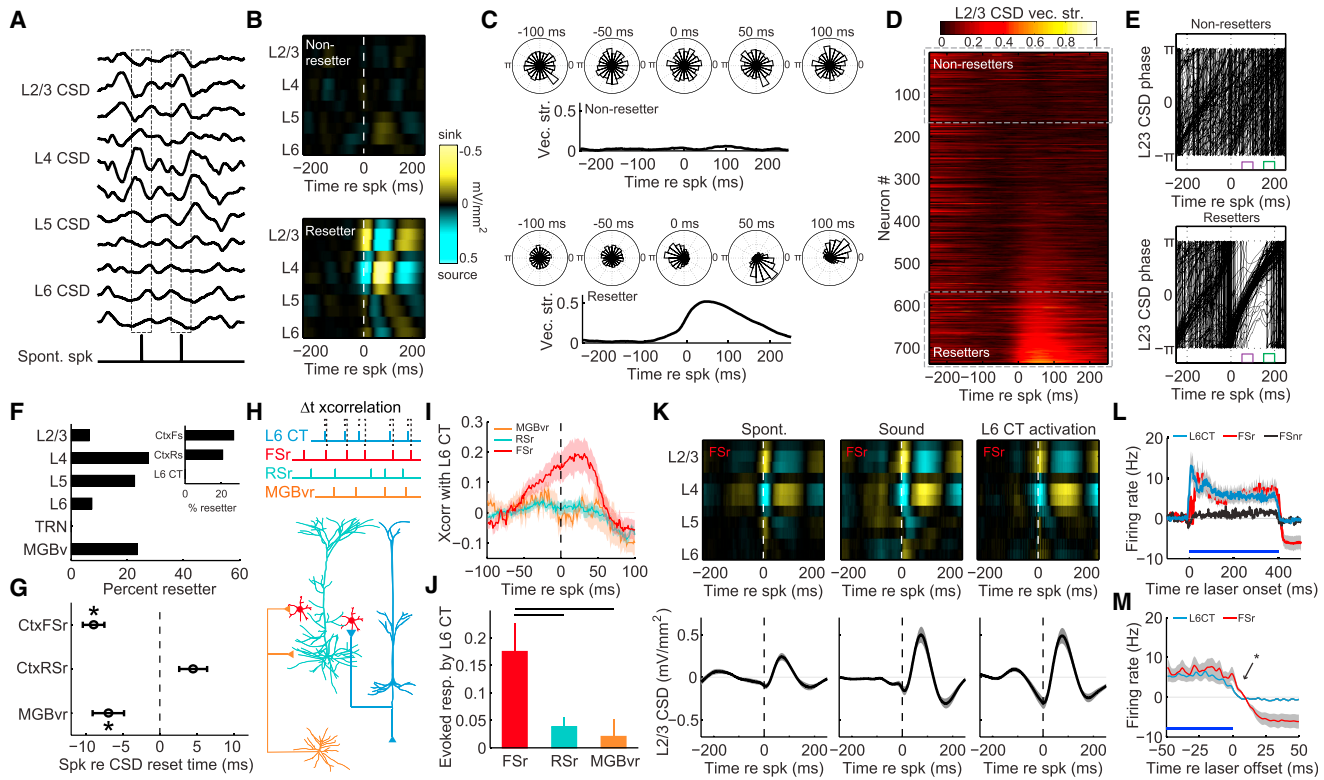


Figure 7. L6 CT Neurons Reset the Phase of Low-Frequency Cortical Rhythms by Driving a Subtype of Cortical Fast-Spiking Interneuron

- (A) Schematic diagram depicting the analysis approach for spike-triggered CSD phase and amplitude.
- (B) Spike-triggered CSD amplitude from two exemplar A1 single units. Spontaneous spikes are associated with a clear pattern of alternating sinks and sources across the cortical column in some single units (a “resetter” unit, bottom), but not others (a “non-resetter” unit, top).
- (C) L2/3 delta-theta CSD phase histograms at discrete time bins before and after spontaneous spikes from the same two single units shown in (B). The L2/3 CSD vector strength represents the phase precision over time.
- (D) Spontaneous spike-triggered phase changes from 723 single units recorded from the thalamus and cortex of awake mice are sorted according to the change in L2/3 CSD vector strength. Resetter units ($n = 184$) were operationally defined as those that increased the post-spike L2/3 CSD vector strength by 0.05 or more.
- (E) Spike-triggered phase histograms from all resetter and 185 non-resetter units. Each trace is the mean phase trajectory from a single unit. Resetter units reset the phase of the L2/3 CSD to π at the time of the spike. The spike-triggered phase remains well organized at the short and long delay intervals following spontaneous resetter spikes (purple = π and green = 0 phase, respectively).
- (F) Histogram of resetter occurrence as a function of brain region and spike waveform.
- (G) Mean (± 1 SEM) latency between spontaneous spike occurrence and the time of CSD reset, operationally defined as the peak negativity in the L2/3 delta-theta CSD waveform. For MGBvr resetter (MGBvr, $n = 52$) and cortical FSr units ($n = 31$), spontaneously occurring spikes occurred significantly earlier than the L2/3 CSD reset, suggesting that they could induce the reset (paired t tests, $p < 0.05$ for both). By contrast, RSr unit spikes ($n = 78$) occurred during or just after the CSD reset event (paired t test, $p = 0.1$).
- (H) Cartoon illustrating the four cell types in the putative CSD reset circuit and the cross-correlation analysis approach.
- (I) Mean (± 1 SEM) cross-correlogram of L6 CT unit spike trains with the other resetter unit types.
- (J) Mean (± 1 SEM) probability that a spike in each resetter type will follow a laser-evoked L6 CT spike. Horizontal lines represent significant differences between FSr-evoked spike probability and other unit types (unpaired t test, $p < 0.05$ after correcting for multiple comparisons).
- (K) FSr-spike-triggered L2/3 CSD amplitude for spike events occurring spontaneously, during auditory stimulation, or during optogenetic activation of L6 CT units. Note similarity of FSr-triggered CSD change and laser-evoked CSD change in Figure 6D.
- (L) Mean (± 1 SEM) laser-evoked firing rate in L6 CT neurons, FSr neurons, and FS neurons not associated with CSD reset (FSnr).
- (M) L6 CT spiking ceases immediately at laser offset, whereas FSr neuron spiking remains significantly higher for at least 10 ms (Wilcoxon rank-sum, $p < 0.05$).

low-frequency CSD rhythm to suppress spiking, sharpen frequency tuning, and improve behavioral frequency discrimination. Although L6 CT unit spiking did not directly reset the CSD, L6 CT units could indirectly generate the delta-theta rhythm by driving MGBvr or CtxFSr units. To address this possibility, we optogenetically phototagged L6 CT neurons and cross-correlated their spike trains with the other resetter neuron types (Figure 7H). There was no consistent relationship be-

tween the spiking of L6 CT neurons and the MGBvr or regular spiking units in A1 (Figure 7I). However, we found a significant correlation between L6 CT neurons and CtxFSr units. L6 CT spikes led CtxFSr spikes by approximately 13 ms, suggesting that L6 CT units could reset the CSD phase by driving CtxFSr units (Figure 7J).

Whether spontaneously occurring, driven by sound, or evoked by optogenetic activation of L6 CT neurons, CtxFSr unit spikes

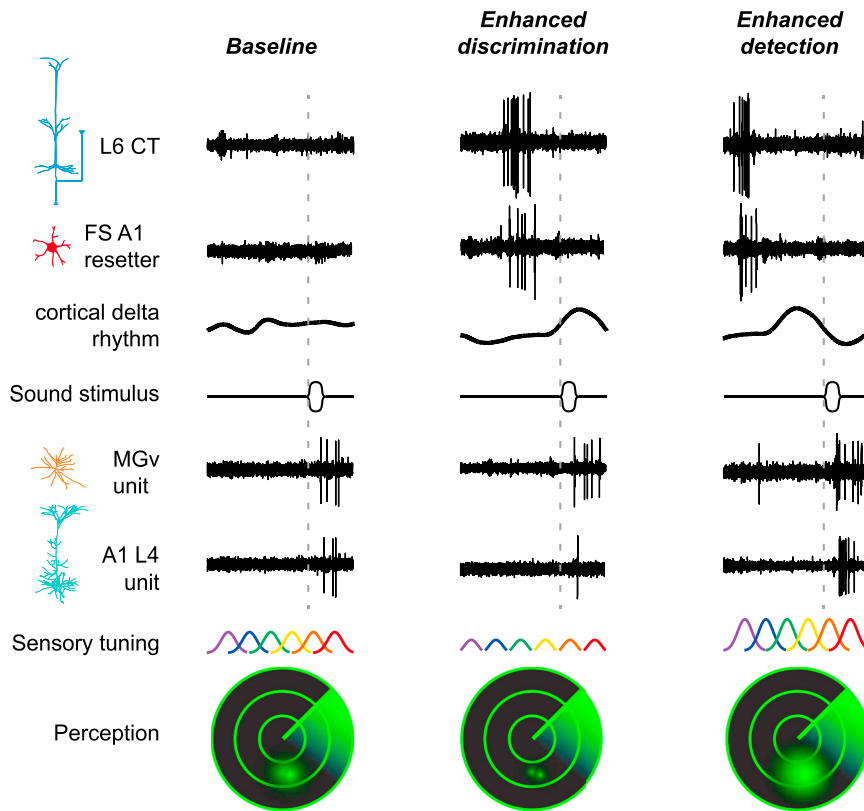


Figure 8. Summary of Findings Supporting a Contribution of L6 CT Neurons to Perceptual Modes of Heightened Detection or Discrimination

Unit recording traces are arranged to illustrate the main effects described in previous figures. Left column: in a baseline condition with minimal spiking activity in L6 CT and FS resetter neurons, the power of low-frequency CSD rhythms is weak, and sound-evoked spiking in thalamic and cortical principal neurons is moderate. Intense firing of L6 CT neurons engages FS resetter interneurons that increase the power and reset the phase of low-frequency rhythms. Middle columns: at short delays following an intense volley of spikes in L6 CT and FS resetter neurons, the induced cortical delta-theta rhythm is at a positive, low-excitability phase, and sound-evoked spikes are suppressed in A1 but in the MGBv. Right column: at longer delays following a volley of spikes in L6 CT and FS resetter neurons, the phase of the cortical delta-theta rhythm has rotated to a negative, high-excitability phase, and sound-evoked spikes are greatly enhanced both in MGBv and A1. Modulating the excitability of cortical neurons has predictable effects on sensory tuning across ensembles of A1 neurons and behavioral measures of sound perception, illustrated as the resolution of two objects on a sonar display. Suppressed sound-evoked A1 activity shortly following the volley of spikes in the cortical reset network dampens excitability but reduces overlap between neighboring tuning functions, supporting enhanced discrimination of sound frequencies but

reduced auditory sensitivity (middle column). Enhanced sound-evoked spiking scales up excitability and increases the overlap between neighboring tuning functions, resulting in enhanced sensitivity to sound at the expense of reduced frequency discriminability (right column).

induced one or two cycles of a low-frequency pattern of electrical sinks and sources in L4 and L2/3 (Figure 7K). Laser stimulation directly activated L6 CT neurons, and their activity was followed shortly thereafter by robust indirect activation of CtxFSr neurons (Figure 7L). Interestingly, L6 CT activation had no effect on cortical FS units whose spontaneous spikes were not associated with a columnar CSD reset (CtxFSnr, Figure 7L). During laser stimulation, when L6 CT and CtxFSr are coactive (as others likely are as well) a high gamma rhythm dominates, and the 2–6 Hz delta-theta rhythm is clearly defined but relatively weak (Figure 6B). L6 CT units cease firing immediately after the laser power falls to zero, yet CtxFSr units continue to spike for a short time thereafter (Figure 7M). Because unopposed CtxFSr spiking induced one to two cycles of the delta-theta rhythm, we surmised that the low-frequency rhythm induced by the abrupt cessation of L6 CT spiking may be generated, in part, from this brief period when CtxFSr unit spiking is unopposed by L6 CT spiking. Therefore, as in V1, L6 CT activation induces divisive suppression by selectively driving cortical FS units that impose strong, feedforward inhibition (Bortone et al., 2014). However, in auditory cortex, divisive suppression occurs only shortly after L6 CT units deactivate and is coincident with a low-frequency electrical rhythm that dampens spontaneous and sound-evoked spiking but enhances frequency discrimination for approximately 100 ms.

DISCUSSION

As summarized in Figure 8, we described a L6 corticothalamic circuit (Figure 1) that can either enhance or suppress spontaneous (Figure 2) or sound-evoked (Figure 3) activity, depending on the timing between A1 spikes and optogenetic activation of L6 CT neurons. We demonstrated that enhanced A1 sound-evoked responses and wider frequency tuning were correlated with improved behavioral sound detection but reduced discrimination accuracy. Conversely, suppressed A1 responses and sharper frequency tuning were associated with improved behavioral sound discrimination but elevated detection thresholds (Figure 4). Interestingly, the strongest modulation of cortical responses and sound perception occurred just after deactivation of L6 CT units rather than during their activation. We found that multiplicative or additive gain in A1 responses at a long interval following L6 CT deactivation could be inherited from a corresponding change in MGBv units, yet we did not observe a thalamic antecedent for the divisive or subtractive gain at short intervals following L6 CT deactivation (Figure 5). To explain the suppressive modulation of auditory responses following the offset of L6 CT activation, we turned to dynamic changes in the frequency and phase of sinks and sources in the local electrical field. We found that L6 CT deactivation reset the phase of delta-theta rhythms such that the low-excitability period of

the CSD was associated with suppressed sound-evoked responses, sharper frequency tuning, and improved discrimination (Figure 6). To identify the neural circuit underlying delta-theta reset, we first characterized hundreds of single neurons with spontaneous spike events associated with strong phase alignment and enhanced low-frequency CSD signal amplitude. Among our heterogeneous sample of resetter neurons, the cortical FS neuron was the only type that spiked before CSD reset, and it was strongly driven by L6 CT neurons (Figure 7). We concluded that the divisive or subtractive gain observed shortly after L6 CT deactivation could be attributed to a delta-theta phase reset that arose from the interaction of L6 CT and cortical FS neurons (see also Carracedo et al., 2013).

Distinct Signatures of Neuromodulation in A1 as Compared to Other Cortical Areas

L6 CTs are glutamate-releasing pyramidal neurons (Bortone et al., 2014; Bourassa and Deschênes, 1995; Zhang and Deschênes, 1997). In V1, the net effect of L6 CT activation is to suppress spiking via disynaptic inhibition from GABAergic FS interneurons (Bortone et al., 2014; Olsen et al., 2012). As an exception to this rule, L6 CT neurons directly excite neurons in L5a in both V1 and barrel cortex, though again, L6 CT activation mediated a net inhibitory effect outside of L5a (Kim et al., 2014). By contrast, the net effect of activating L6 CT neurons in all layers of A1 is excitatory. This sign reversal seems unlikely to simply reflect the absence of disynaptic inhibition evoked by L6 CT neurons, as we also observed strong activation of FS “resetting” interneurons during laser stimulation, (Figure 7L). Apparently, in A1, the combined effect of feedforward excitatory inputs from the L6 CTs and disynaptic inhibition from CtxFSr neurons tips toward net excitation across the column, while in V1 it tips toward net suppression. This may reflect subtle but important differences in the set point of local inhibitory networks between the two brain areas, as has also been suggested from the opposite effects of locomotion on sensory-evoked responses in A1 and V1 (Fu et al., 2014; McGinley et al., 2015; Niell and Stryker, 2010; Schneider et al., 2014; Zhou et al., 2014).

In many respects, A1 suppression at a short delay following L6 CT deactivation resembled the modulation in V1 during L6 CT activation: the modulation had a clear divisive component associated with strong activation a specialized subtype of FS interneuron (Olsen et al., 2012). In V1, L6 CT neurons suppress visual processing throughout the column by driving L6 FS interneurons with vertically oriented, translaminal axon fields (Bortone et al., 2014). In A1, the suppressive effect of L6 CT deactivation was also specific to a subtype of FS interneuron (Figure 7L) that changed network excitability across the entire column, though there was no indication in our data that these FS neurons were restricted to L6 (Figure 7G).

A L6 CT Circuit for Resetting the Phase of Low-Frequency Rhythms and Dynamically Regulating Stimulus Salience

Expectation can rise and fall over time. Stimuli that arrive at expected intervals are more rapidly and accurately processed than stimuli that occur at unexpected intervals (Buran et al., 2014; Jarmanillo and Zador, 2011; Jones et al., 2002; Nobre et al., 2007;

Wright and Fitzgerald, 2004). A time-dependent modulation of neural and perceptual salience may arise from fluctuations in the underlying low-frequency cortical electric field not only because perceptual salience is modulated by oscillation phase, but because phase itself can be proactively controlled through attention and expectation (Luo and Poeppel, 2007; Schroeder and Lakatos, 2009). By resetting the phase at opportune moments, attended stimulus features can benefit from enhanced processing at the high-excitability phase of an oscillation, and distractors can be suppressed by aligning the timing of their occurrence to the low-excitability phase (Henry and Obleser, 2012; Lakatos et al., 2008). By resetting the phase of nested cortical oscillators, the temporal signature of a target speaker can be perceptually enhanced and neurophysiologically segregated from the temporal signature of a competing speaker’s speech (Ghitza, 2011; Giraud and Poeppel, 2012; Giraud et al., 2007; Zion Golumbic et al., 2013). Modulation through phase entrainment is not only achieved in time, but also in space; for example, attending to a stream of tones at a fixed frequency while ignoring distractor tones at another frequency sets up regional pockets of low-frequency oscillations in which the high-excitability region is in phase throughout the target region of the tonotopic map but in counter-phase in map regions that encode distractor frequencies (Lakatos et al., 2013; O’Connell et al., 2014).

While there is general agreement that the phase of ongoing delta and theta oscillations can be adaptively reset either through high-contrast, bottom-up stimulus features or through top-down, executive control signals, the neural mechanism of phase reset is unknown. By computing the spike-triggered phase for hundreds of individual neurons, we identified a subnetwork of neurons distributed throughout middle and deep layers of the A1 column and MGB that exert a strong influence over the amplitude and phase of delta-theta rhythms. This analysis suggested two overlapping networks: first, a bottom-up network involving neurons in the MGBv and cortical FS neurons that reset the phase shortly following the onset of a tone close to their preferred frequency; and second, a separate network also involving cortical FS neurons that are driven by L6 CT neurons. As an essential node in a deep-layer modulatory circuit, L6 CT neurons may be able to resolve the competing demands of detection and discrimination by coordinating their spiking at opportune moments during analysis of a sensory scene. In this regard, it is not surprising that the strongest effects of L6 CT activation on sensory processing and perception occurred after a volley of L6 CT spikes had ended rather than while L6 CTs were activated. Anticipatory listening would require some form of structured neural activity to reliably precede predicted inputs. Future work will determine whether L6 CT neurons fulfill that role.

STAR★METHODS

Detailed methods are provided in the online version of this paper and include the following:

- KEY RESOURCES TABLE
- CONTACT FOR REAGENT AND RESOURCE SHARING
- EXPERIMENTAL MODEL AND SUBJECT DETAILS

● METHODS DETAILS

- Virus-Mediated Gene Delivery
- Preparation for Awake, Head-Fixed Recordings
- Neurophysiology
- Optogenetic and Acoustic Stimulation for Neurophysiology Recordings
- Analysis of Extracellular Unit Recordings
- Analysis of the Local Field Potential and Current Source Density
- Chronic Optic Fiber Implantation
- Behavioral Training and Testing
- Anatomy

● QUANTIFICATION AND STATISTICAL ANALYSIS

● DATA AND SOFTWARE AVAILABILITY

SUPPLEMENTAL INFORMATION

Supplemental Information includes four figures and one table and can be found with this article online at <http://dx.doi.org/10.1016/j.neuron.2017.05.019>.

AUTHOR CONTRIBUTIONS

W.G. and A.B.-M. collected data. A.R.C. performed pilot experiments. W.G. analyzed the data. W.G., A.R.C., and D.B.P. designed the experiments. W.G. and D.B.P. wrote the manuscript.

ACKNOWLEDGMENTS

We thank Ken Hancock for support with data collection software. A Tesla K20 GPU was donated to W.G. by the NVIDIA Corporation. This work was supported by NIH grant R21012894 (D.B.P.) and a HHMI international student research fellowship (W.G.).

Received: September 8, 2016

Revised: March 3, 2017

Accepted: May 9, 2017

Published: June 15, 2017

REFERENCES

- Bortone, D.S., Olsen, S.R., and Scanziani, M. (2014). Translaminar inhibitory cells recruited by layer 6 corticothalamic neurons suppress visual cortex. *Neuron* 82, 474–485.
- Bourassa, J., and Deschênes, M. (1995). Corticothalamic projections from the primary visual cortex in rats: a single fiber study using biocytin as an anterograde tracer. *Neuroscience* 66, 253–263.
- Briggs, F., Kiley, C.W., Callaway, E.M., and Usrey, W.M. (2016). Morphological substrates for parallel streams of corticogeniculate feedback originating in both V1 and V2 of the macaque monkey. *Neuron* 90, 388–399.
- Buran, B.N., von Trapp, G., and Sanes, D.H. (2014). Behaviorally gated reduction of spontaneous discharge can improve detection thresholds in auditory cortex. *J. Neurosci.* 34, 4076–4081.
- Carracedo, L.M., Kjeldsen, H., Cunnington, L., Jenkins, A., Schofield, I., Cunningham, M.O., Davies, C.H., Traub, R.D., and Whittington, M.A. (2013). A neocortical delta rhythm facilitates reciprocal interlaminar interactions via nested theta rhythms. *J. Neurosci.* 33, 10750–10761.
- Crandall, S.R., Cruikshank, S.J., and Connors, B.W. (2015). A corticothalamic switch: controlling the thalamus with dynamic synapses. *Neuron* 86, 768–782.
- David, S.V., Fritz, J.B., and Shamma, S.A. (2012). Task reward structure shapes rapid receptive field plasticity in auditory cortex. *Proc. Natl. Acad. Sci. USA* 109, 2144–2149.
- Denman, D.J., and Contreras, D. (2015). Complex effects on in vivo visual responses by specific projections from mouse cortical layer 6 to dorsal lateral geniculate nucleus. *J. Neurosci.* 35, 9265–9280.
- Froemke, R.C., Carcea, I., Barker, A.J., Yuan, K., Seybold, B.A., Martins, A.R.O., Zaika, N., Bernstein, H., Wachs, M., Levis, P.A., et al. (2013). Long-term modification of cortical synapses improves sensory perception. *Nat. Neurosci.* 16, 79–88.
- Fu, Y., Tucciarone, J.M., Espinosa, J.S., Sheng, N., Darcy, D.P., Nicoll, R.A., Huang, Z.J., and Stryker, M.P. (2014). A cortical circuit for gain control by behavioral state. *Cell* 156, 1139–1152.
- Ghitza, O. (2011). Linking speech perception and neurophysiology: speech decoding guided by cascaded oscillators locked to the input rhythm. *Front. Psychol.* 2, 130.
- Giraud, A.-L., and Poeppel, D. (2012). Cortical oscillations and speech processing: emerging computational principles and operations. *Nat. Neurosci.* 15, 511–517.
- Giraud, A.L., Kleinschmidt, A., Poeppel, D., Lund, T.E., Frackowiak, R.S.J., and Laufs, H. (2007). Endogenous cortical rhythms determine cerebral specialization for speech perception and production. *Neuron* 56, 1127–1134.
- Gong, S., Doughty, M., Harbaugh, C.R., Cummins, A., Hatten, M.E., Heintz, N., and Gerfen, C.R. (2007). Targeting Cre recombinase to specific neuron populations with bacterial artificial chromosome constructs. *J. Neurosci.* 27, 9817–9823.
- Guo, W., Hight, A.E., Chen, J.X., Klapoetke, N.C., Hancock, K.E., Shinn-Cunningham, B.G., Boyden, E.S., Lee, D.J., and Polley, D.B. (2015). Hearing the light: neural and perceptual encoding of optogenetic stimulation in the central auditory pathway. *Sci. Rep.* 5, 10319.
- Hackett, T.A., Barkat, T.R., O'Brien, B.M.J., Hensch, T.K., and Polley, D.B. (2011). Linking topography to tonotopy in the mouse auditory thalamocortical circuit. *J. Neurosci.* 31, 2983–2995.
- Hackett, T.A., Clause, A.R., Takahata, T., Hackett, N.J., and Polley, D.B. (2016). Differential maturation of vesicular glutamate and GABA transporter expression in the mouse auditory forebrain during the first weeks of hearing. *Brain Struct. Funct.* 221, 2619–2673. Published online July 10, 2015.
- Henry, M.J., and Obleser, J. (2012). Frequency modulation entrains slow neural oscillations and optimizes human listening behavior. *Proc. Natl. Acad. Sci. USA* 109, 20095–20100.
- Ito, T., Bishop, D.C., and Oliver, D.L. (2011). Expression of glutamate and inhibitory amino acid vesicular transporters in the rodent auditory brainstem. *J. Comp. Neurol.* 519, 316–340.
- Jaramillo, S., and Zador, A.M. (2011). The auditory cortex mediates the perceptual effects of acoustic temporal expectation. *Nat. Neurosci.* 14, 246–251.
- Jones, E.G. (2007). *The Thalamus* (Cambridge University Press).
- Jones, M.R., Moynihan, H., MacKenzie, N., and Puente, J. (2002). Temporal aspects of stimulus-driven attending in dynamic arrays. *Psychol. Sci.* 13, 313–319.
- Kajikawa, Y., and Schroeder, C.E. (2011). How local is the local field potential? *Neuron* 72, 847–858.
- Kaur, S., Rose, H.J., Lazar, R., Liang, K., and Metherate, R. (2005). Spectral integration in primary auditory cortex: laminar processing of afferent input, in vivo and in vitro. *Neuroscience* 134, 1033–1045.
- Kayser, C., Wilson, C., Safaai, H., Sakata, S., and Panzeri, S. (2015). Rhythmic auditory cortex activity at multiple timescales shapes stimulus-response gain and background firing. *J. Neurosci.* 35, 7750–7762.
- Kim, J., Matney, C.J., Blankenship, A., Hestrin, S., and Brown, S.P. (2014). Layer 6 corticothalamic neurons activate a cortical output layer, layer 5a. *J. Neurosci.* 34, 9656–9664.
- Kuchibhotla, K.V., Gill, J.V., Lindsay, G.W., Papadoyannis, E.S., Field, R.E., Sten, T.A.H., Miller, K.D., and Froemke, R.C. (2017). Parallel processing by cortical inhibition enables context-dependent behavior. *Nat. Neurosci.* 20, 62–71. Published online October 31, 2016.

- Lakatos, P., Karmos, G., Mehta, A.D., Ulbert, I., and Schroeder, C.E. (2008). Entrainment of neuronal oscillations as a mechanism of attentional selection. *Science* *320*, 110–113.
- Lakatos, P., Musacchia, G., O’Connell, M.N., Falchier, A.Y., Javitt, D.C., and Schroeder, C.E. (2013). The spectrotemporal filter mechanism of auditory selective attention. *Neuron* *77*, 750–761.
- Lee, C.C., Lam, Y.-W., and Sherman, S.M. (2012). Intracortical convergence of layer 6 neurons. *Neuroreport* *23*, 736–740.
- Letzkus, J.J., Wolff, S.B.E., Meyer, E.M.M., Tovote, P., Courtin, J., Herry, C., and Lüthi, A. (2011). A disinhibitory microcircuit for associative fear learning in the auditory cortex. *Nature* *480*, 331–335.
- Llano, D.A., and Sherman, S.M. (2008). Evidence for nonreciprocal organization of the mouse auditory thalamocortical-corticothalamic projection systems. *J. Comp. Neurol.* *507*, 1209–1227.
- Luo, H., and Poeppel, D. (2007). Phase patterns of neuronal responses reliably discriminate speech in human auditory cortex. *Neuron* *54*, 1001–1010.
- Marlin, B.J., Mitre, M., D’amour, J.A., Chao, M.V., and Froemke, R.C. (2015). Oxytocin enables maternal behaviour by balancing cortical inhibition. *Nature* *520*, 499–504.
- McGinley, M.J., David, S.V., and McCormick, D.A. (2015). Cortical membrane potential signature of optimal states for sensory signal detection. *Neuron* *87*, 179–192.
- Mease, R.A., Krieger, P., and Groh, A. (2014). Cortical control of adaptation and sensory relay mode in the thalamus. *Proc. Natl. Acad. Sci. USA* *111*, 6798–6803.
- Mesgarani, N., and Chang, E.F. (2012). Selective cortical representation of attended speaker in multi-talker speech perception. *Nature* *485*, 233–236.
- Müller-Preuss, P., and Mitzdorf, U. (1984). Functional anatomy of the inferior colliculus and the auditory cortex: current source density analyses of click-evoked potentials. *Hear. Res.* *16*, 133–142.
- Niell, C.M., and Stryker, M.P. (2010). Modulation of visual responses by behavioral state in mouse visual cortex. *Neuron* *65*, 472–479.
- Nobre, A., Correa, A., and Coull, J. (2007). The hazards of time. *Curr. Opin. Neurobiol.* *17*, 465–470.
- O’Connell, M.N., Falchier, A., McGinnis, T., Schroeder, C.E., and Lakatos, P. (2011). Dual mechanism of neuronal ensemble inhibition in primary auditory cortex. *Neuron* *69*, 805–817.
- O’Connell, M.N., Barczak, A., Schroeder, C.E., and Lakatos, P. (2014). Layer specific sharpening of frequency tuning by selective attention in primary auditory cortex. *J. Neurosci.* *34*, 16496–16508.
- Olsen, S.R., Bortone, D.S., Adesnik, H., and Scanziani, M. (2012). Gain control by layer six in cortical circuits of vision. *Nature* *483*, 47–52.
- Phillips, E.A.K., and Hasenstaub, A.R. (2016). Asymmetric effects of activating and inactivating cortical interneurons. *eLife* *5*, e18383.
- Pi, H.J., Hangya, B., Kvitsiani, D., Sanders, J.J., Huang, Z.J., and Kepecs, A. (2013). Cortical interneurons that specialize in disinhibitory control. *Nature* *503*, 521–524.
- Pinto, L., Goard, M.J., Estandian, D., Xu, M., Kwan, A.C., Lee, S.-H., Harrison, T.C., Feng, G., and Dan, Y. (2013). Fast modulation of visual perception by basal forebrain cholinergic neurons. *Nat. Neurosci.* *16*, 1857–1863.
- Polley, D.B., Steinberg, E.E., and Merzenich, M.M. (2006). Perceptual learning directs auditory cortical map reorganization through top-down influences. *J. Neurosci.* *26*, 4970–4982.
- Schneider, D.M., Nelson, A., and Mooney, R. (2014). A synaptic and circuit basis for corollary discharge in the auditory cortex. *Nature* *513*, 189–194.
- Schroeder, C.E., and Lakatos, P. (2009). Low-frequency neuronal oscillations as instruments of sensory selection. *Trends Neurosci.* *32*, 9–18.
- Seybold, B.A., Phillips, E.A.K., Schreiner, C.E., and Hasenstaub, A.R. (2015). Inhibitory actions unified by network integration. *Neuron* *87*, 1181–1192.
- Sherman, S.M., and Guillery, R.W. (2002). The role of the thalamus in the flow of information to the cortex. *Philos. Trans. R. Soc. Lond. B Biol. Sci.* *357*, 1695–1708.
- Shuler, M.G.H., and Bear, M.F. (2006). Reward timing in the primary visual cortex. *Science* *311*, 1606–1609.
- Sohoglu, E., and Chait, M. (2016). Detecting and representing predictable structure during auditory scene analysis. *eLife* *5*, 1–17.
- Temereanca, S., and Simons, D.J. (2004). Functional topography of corticothalamic feedback enhances thalamic spatial response tuning in the somatosensory whisker/barrel system. *Neuron* *41*, 639–651.
- Winer, J.A., Diehl, J.J., and Larue, D.T. (2001). Projections of auditory cortex to the medial geniculate body of the cat. *J. Comp. Neurol.* *430*, 27–55.
- Wright, B.A., and Fitzgerald, M.B. (2004). The time course of attention in a simple auditory detection task. *Percept. Psychophys.* *66*, 508–516.
- Zhang, Z.W., and Deschênes, M. (1997). Intracortical axonal projections of lamina VI cells of the primary somatosensory cortex in the rat: a single-cell labeling study. *J. Neurosci.* *17*, 6365–6379.
- Zhou, M., Liang, F., Xiong, X.R., Li, L., Li, H., Xiao, Z., Tao, H.W., and Zhang, L.I. (2014). Scaling down of balanced excitation and inhibition by active behavioral states in auditory cortex. *Nat. Neurosci.* *17*, 841–850.
- Zion Golumbic, E.M., Ding, N., Bickel, S., Lakatos, P., Schevon, C.A., McKhann, G.M., Goodman, R.R., Emerson, R., Mehta, A.D., Simon, J.Z., et al. (2013). Mechanisms underlying selective neuronal tracking of attended speech at a “cocktail party”. *Neuron* *77*, 980–991.

STAR★METHODS

KEY RESOURCES TABLE

REAGENT or RESOURCE	SOURCE	IDENTIFIER
Antibodies		
Rabbit anti-NeuN	abcam	ab104225; RRID: AB_10711153
Alexa fluor 405 (goat anti-rabbit IgG)	abcam	ab175652
Bacterial and Virus Strains		
AAV5-EF1 α -DIO-hChr2(E123T/T159C)-mCherry	UNC Vector Core	AV4559
AAV5-CAG-FLEX-ArchT-tdTomato	UNC Vector Core	AV4567bc
AAV5-FLEX-tdTomato	UNC Vector Core	AV4599
Biological Samples		
Chemicals, Peptides, and Recombinant Proteins		
Ketamine hydrochloride	Vedco	NDC 50989-161-06
Xylazine	Bayer Animal Health	CAS 7361-61-7
Lidocaine hydrochloride	Hospira Inc.	Lot 71-157-DK
Buprenorphine hydrochloride	Buprenex	NDC 12496-0757-5
Green retrobeads	LumaFluor	<i>Green Retrobeads IX (100 μl)</i>
Isoflurane	Piramal	NDC 66794-013-10
Flow-It ALC Flowable Composite	Pentron	N11B
Experimental Models: Organisms/Strains		
Mouse: Ntsr1-Cre	GENSAT	B6.FVB(Cg)-Tg(Ntsr1-Cre)GN220Gsat/Mmcd
Mouse: Ai32	The Jackson Laboratory	B6;129S-Gt(ROSA) ^{tm32(CAG-COP4⁺H134R/EYFP)} Hze/J Jax Stock #: 012569
Mouse: Ai14	The Jackson Laboratory	B6;129S6-Gt(ROSA) ^{tm14(CAG-tdTomato)} Hze/J; Jax Stock #: 007908
Mouse: PV-Cre	The Jackson Laboratory	B6;129P2-Pvalb ^{tm1(cre)Arbr} /J Jax Stock #: 008069
Mouse: ChAT-Cre	The Jackson Laboratory	B6;129S6-Chat ^{tm2(cre)Lowl} /J Jax Stock #: 006410
Mouse: CBA/CaJ	The Jackson Laboratory	CBA/CaJ Jax Stock #: 000654
Software and Algorithms		
MATLAB 2013b	Mathworks	
Labview 2015	National Instruments	
Wave_clus		http://www2.le.ac.uk/departments/engineering/research/bioengineering/neuroengineering-lab/spike-sorting
Other		
Linear silicone recording electrode	NeuroNexus	NeuroNexus A1x16-100-177-3mm
Linear silicone recording electrode	NeuroNexus	NeuroNexus A1x16-50-177-5mm
Chronic optic fiber	NeuroNexus	NeuroNexus NNC 1.5mm
Plate Clamps	Altechna	4PC69
Diode laser (473 nm)	Omicron	LuxX [®] 473-100
DPSS laser (532 nm)	LaserGlow	LRS-0532
BioAmp processor	Tucker-Davis Technologies	RZ5D
Free-field Electrostatic speaker	Tucker-Davis Technologies	ES1
PXI Controller	National Instruments	PXIe-8840

CONTACT FOR REAGENT AND RESOURCE SHARING

Requests for further information should be directed to and will be fulfilled by the Lead Contact, Daniel Polley (daniel_polley@meei.harvard.edu).

EXPERIMENTAL MODEL AND SUBJECT DETAILS

All procedures were approved by the Massachusetts Eye and Ear Infirmary Animal Care and Use Committee and followed the guidelines established by the National Institutes of Health for the care and use of laboratory animals. Both male and female mice were used in this study. All mice were maintained under light (7am – 7pm) and dark (7pm – 7am) cycle conditions with ad libitum access to food and water. Animals chronically implanted with headplates were housed individually. Age-matched litter mates were randomly assigned to experimental groups.

For L6 CT experiments, we used 58 hemizygous *Ntsr1-Cre* transgenic mice, aged 6–12 weeks (B6.FVB(Cg)-Tg(*Ntsr1-Cre*)GN220Gsat/Mmcd). For comparisons of laser-evoked cortical activity from other cell types, we used an additional two PV-*Cre:Ai32* mice, two ChAT-*Cre:Ai32* mice, and two wild-type mice expressing CamKII α -hChR2.

METHODS DETAILS

Virus-Mediated Gene Delivery

Mice of either sex aged 6–7 weeks were anesthetized with ketamine (100 mg/kg) and xylazine (10 mg/kg). A surgical plane of anesthesia was maintained throughout the procedure with supplements of ketamine (50 mg/kg) as needed. The animal's body temperature was maintained near 36.5°C using a homeothermic blanket system (Fine Science Tools). The surgical area was numbed with a subcutaneous injection of lidocaine (5 mg/mL). An incision was made on the right side of the scalp to expose the skull around the caudal end of the temporal ridge, where the caudomedial end of the temporalis muscle joins to the skull. The temporal ridge provides a reliable cranial landmark for core fields of the auditory cortex. We made 2–3 burr holes along the temporal ridge, spanning a region 1.0–2.0 mm rostral to the lambdoid suture. At each burr hole, 0.3–0.5 μ L of either AAV5-EF1 α -DIO-hChR2(E123T/T159C)-mCherry, AAV5-CAG-FLEX-ArchT-tdTomato or AAV5-FLEX-tdTomato solution was injected into the cortex 450 μ m below the pial surface at 0.05–0.1 μ L/min using a motorized injector (Stoelting Co.). For animals undergoing behavioral assessments, 0.6 μ L of virus solution was injected into both the left and right auditory cortex. Following the procedure, antibiotic ointment was applied to the wound margin and an analgesic was administered (Buprenex, 0.05 mg/kg). Neurophysiology and behavior experiments began 3–4 weeks following virus injection.

Preparation for Awake, Head-Fixed Recordings

Mice were once again brought to a surgical plane of anesthesia, using the same protocol for general anesthesia, local anesthesia and body temperature control described above. The periosteum overlying the dorsal surface of the skull was thoroughly removed. The skull surface was prepared with 70% ethanol and etchant (C & B Metabond). A titanium head plate was then cemented to the skull, centered on Bregma. After recovery, animals were housed individually. Animals were given at least 48 hr to acclimate to the head plate before any further experiments.

Before the first recording session, animals were briefly anesthetized with isoflurane (1.5% in oxygen) while a small craniotomy (0.5 \times 1.0 mm, medial-lateral \times rostral-caudal) was made along the caudal end of the right temporal ridge, 1 mm rostral to the lambdoid suture to expose A1. A small chamber was built around the craniotomy with UV-cured cement and filled with ointment. At the end of each recording session, the chamber was flushed, filled with fresh ointment, and sealed with UV-cured cement. The chamber was removed and rebuilt under isoflurane anesthesia before each subsequent recording session. Typically, 4–7 recording sessions were performed on each animal over the course of 1–2 weeks. For dual A1/MGB or A1/TRN recordings, a second craniotomy and chamber provided access to the MGB (1 mm rostral to the lambdoid suture, 2–3 mm lateral to midline) or the TRN (2 mm rostral to the MGB craniotomy).

Neurophysiology

On the day of recording, the head was immobilized by attaching the head plate to a rigid clamp (Altechna). The body rested atop a disk, coated with a sound-attenuating polymer that was mounted on a low-friction, silent rotor. We continuously monitored the eyelid and status of the rotating disk to confirm that all recordings were made in the awake condition.

For columnar recordings, a single-shank linear silicon probe (NeuroNexus A1x16-100-177-3mm) was inserted into the auditory cortex craniotomy perpendicular to the brain surface using a micromanipulator (Narishige) and a hydraulic microdrive (FHC) with the tip of the probe positioned approximately 1.3 mm below the brain surface, such that the top 2 electrode contacts were outside the brain, the bottom 2 contacts were in the white matter or hippocampus, and the middle 11–12 contacts spanned all six layers of the auditory cortex. At the beginning of the first recording session, several penetrations were made along the caudal-rostral extent of the craniotomy to locate the high-frequency reversal of the tonotopic gradient that demarcates the rostral boundary of mouse A1 ([Hackett et al., 2011](#)). For dual recordings, a second silicon probe (NeuroNexus A1X16-50-177-5mm) was inserted into MGB or TRN using a

dorsal approach. To identify the MGBv on any given day of recording, we first recorded lateral to the MGB, in the hippocampus, and then progressively marched the electrode medial in 0.1mm steps until we had at least eight contiguous channels with noise-evoked spiking activity. By validating this approach in pilot experiments through electrolytic lesion reconstructions in post-mortem tissue (data not shown), we were assured of recording from the lateral bank of the MGB, which contains the MGBv and, depending on the caudal-rostral coordinates, might also contain recording sites in the dorsal subdivision or supragenulate nucleus (Hackett et al., 2011). MGBv recordings were limited to the most ventral recordings sites (2.6–3.0 mm below the brain surface) to exclude recordings from the dorsal subdivision or supragenulate nucleus. For TRN recordings, units were classified as putative auditory TRN units only if they were both sound responsive and exhibited a thin spike waveform (peak-to-trough delay less than 0.4 ms, Figure S2C). Based on the frequency tuning of the recorded MGB or TRN units, the location of the cortical probe was positioned within the A1 tonotopic gradient to maximize the overlap between cortical and thalamic receptive fields (Figure 5c).

Optogenetic and Acoustic Stimulation for Neurophysiology Recordings

Digital waveforms for the laser command signal and acoustic stimuli were generated with a 24-bit digital-to-analog converter (PXI, National Instruments) using scripts programmed in MATLAB (MathWorks) and LabVIEW (National Instruments). Stimuli were presented via a free-field electrostatic speaker positioned 10cm from left ear canal (Tucker-Davis Technologies). Free-field stimuli were calibrated before recording using a wide-band ultrasonic acoustic sensor (Knowles Acoustics, model SPM0204UD5). The optical signal was generated with a calibrated 473 nm diode laser for ChR2 experiments (LuxX, Omicron) or a 532 nm DPSS laser for ArchT experiments (LaserGlow), coupled to an optic fiber. The fiber tip was positioned approximately 1cm above the exposed surface of A1.

Once the silicon probe was positioned in an A1 column, we estimated the laminar position of each electrode from the CSD pattern evoked by broadband noise bursts (50 ms duration, 4 ms onset/offset cosine ramps, 1 s interstimulus interval, 70 dB SPL, 100 repetitions; see analysis of local field potential and current source density). Frequency response areas (FRAs) from all recording sites were delineated from pure tone pips (50 ms duration, 4 ms onset/offset cosine ramps, 0.5 s interstimulus interval, 4–45 kHz with 0.1 octave steps, 0–60 dB SPL with 5 dB steps, 2 repetitions of each stimulus, pseudorandomized). Based on the FRAs of all recorded units across layers, we chose a single suprathreshold sound level, normally 40–60 dB SPL, for subsequent measures of the iso-level frequency tuning function. We activated or inactivated L6 CT neurons using laser light at various intensities (400 ms duration, 2 s interstimulus interval, 5–50 mW at the fiber tip in 5 mW steps, 10 repetitions of each stimulus, pseudorandomized). Laser power at the fiber tip was calibrated with a power meter (Thorlabs). The effective laser power at a given point in the cortex was lower than the level calibrated at the optic fiber tip.

To investigate the modulatory effect of L6 CT neuronal activity on columnar sound processing, L6 CT neurons were activated with laser (either 400 ms or 50 ms duration, 3.5 s inter-stimulus interval, either at 20 mW or 5mW above the minimally effective laser power), while pure tone stimuli were presented alone or at various delays with respect to the onset of the laser stimulus (0–800 ms in 50 ms steps, 15 repetitions of each delay, pseudorandomized with a 2 s interval separating each trial). In a subset of experiments described in Figures 6D–6E, we varied the duration of the laser stimuli (10 – 400 ms in octave steps) while holding the intensity constant (20 mW).

Analysis of Extracellular Unit Recordings

Raw signals were digitized at 32-bit, 24.4 kHz (RZ5 BioAmp Processor; Tucker-Davis Technologies) and stored in binary format. In order to eliminate potential movement-generated artifacts, the common mode signal (channel-averaged neural traces) was subtracted from all channels. In experiments where simultaneous recordings were made from probes in cortex and thalamus, the common mode removal was performed separately for each probe. Electrical signals were notch filtered at 60Hz, then band-pass filtered (300–3000 Hz, second order Butterworth filters), from which the multiunit activity (MUA) was extracted as negative deflections in the electrical trace with an amplitude exceeding 4 s.d. of the baseline hash. Single units were separated from the MUA using a wavelet-based spike sorting package (wave_clus). Single unit isolation was confirmed based on the inter-spike-interval histogram (less than 3% of the spikes in the 0–3 ms bins) and the consistency of the spike waveform (s.d of peak-to-trough delay of spikes within the cluster less than 0.2 ms). The average trough-to-peak delay from each single unit formed a clear bimodal distribution (Figure S2), allowing us to further divide our recordings into fast-spiking and regular-spiking units (FS units < than 0.4 ms; RS units > 0.4 ms).

Frequency tuning from MUA or single unit recordings was quantified as the average evoked firing rate measured 10–60 ms following tone onset. By fitting a linear regression model between the tone-evoked firing rates in the tone-alone and the tone plus laser conditions, we could estimate the type of modulation from the slope and the y-intercept of the linear fit. The slope indicates the multiplicative gain of the change; the y-intercept indicates the baseline offset. Only the y-intercept values were used if data was not well fit by linear regression ($p > 0.05$). The cross-correlograms between simultaneously recorded SUs were calculated with up to 250 ms lag time. If neuron A's activity consistently leads neuron B's, the peak of their cross-correlogram had a positive lag time. Therefore, we computed the averaged cross-correlation between 0–50 ms to estimate the direct excitatory drive from neuron A to neuron B.

Analysis of the Local Field Potential and Current Source Density

To extract local field potentials, raw signals were notch filtered at 60 Hz and down-sampled to 1000 Hz. To eliminate potential artifacts introduced by impedance mismatching across recording channels, signals were spatially smoothed along the channels with a triangle filter (5-point Hanning window). The CSD was calculated as the second spatial derivative of the local field potential signal. The frequency components of the CSD signal were analyzed by calculating the Thomson's multitaper power spectral density estimate. For each trial, a set of three spectra were each estimated from three 400-ms windows (0-400 ms before laser, during the 400 ms laser, and 0-400 ms following laser offset). The spectral gain during laser and after laser were calculated using the before-laser spectrum as the baseline.

Noise-evoked columnar CSD patterns were used to determine the location of the A1 recording channel. Two CSD signatures were used to identify L4: A brief current sink first occurs approximately 10 ms after the noise onset, which was used to determine the lower border of L4 (Kaur et al., 2005). A triphasic CSD pattern (sink-source-sink from upper to lower channels) occurs between 20 ms and 50 ms, where the border between the upper sink and the source was used to define the upper boundary of L4. Normally, 2 channels were assigned to L4. Other layers were defined relative to the location of L4 (L2/3: 3 channels above L4; L5: 3 channels below L4; L6: 3 channels below L5). CSD-derived layer assignments were cross-validated against sound-evoked MUA response patterns, where L4 and L5 units responded with higher firing rates and shorter latency. CSD traces were bandpass filtered (2–6 Hz, 2nd order Butterworth filters) to obtain the activity in the delta-theta band. The temporal delay caused by filtering was identified using the cross-correlogram between the original and filtered CSDs, and corrected by time-shifting the filtered signal. The instantaneous phase and amplitude of the CSD were calculated from its analytical signal using the Hilbert transform.

To calculate spike-triggered CSD amplitude, we computed the average columnar CSD waveform 250 ms before and after a spike occurrence for a reference single unit. Spike-triggered CSD phase was computed similarly, except that phase trajectories in the delta-theta band were analyzed rather than CSD amplitude. To classify single units as resetters or non-resetters, we compiled a histogram of the spike-triggered L2/3 CSD phase trajectories 100 ms before and after a reference spike. We then calculated the vector strength for each distribution and operationally defined resetters as single units associated with an increase in vector strength ≥ 0.05 ($n = 184$ single units). The phase delay of any resetter neuron was defined as the lag time between the spike and the trough of the first current sink in the L2/3 CSD.

Chronic Optic Fiber Implantation

Once mice were brought to a stable anesthetic plane, we positioned an implantable optic fiber assembly atop craniotomies made over the left and right auditory cortex ($n = 5$ mice). The fiber tips were lowered until they rested on the brain surface before the assemblies were fixed into place with dental cement (C & B Metabond). The animals were given buprenex and antibiotic ointment post operation. At least 48 hr of recovery time were given before any experiment were performed on implanted animals.

Behavioral Training and Testing

Behavioral testing occurred in an acoustically transparent enclosure (20 × 15 × 30 cm, L × W × H) bisected into two virtual zones resting atop electrified flooring (8 pole scrambled shocker, Coulbourn Instruments). Mouse position was tracked with a commercial webcam. The acoustic, laser, and foot-shock signals were all generated on a National Instruments PXI system using scripts programmed in LabVIEW. Auditory stimuli were delivered through a calibrated free-field speaker positioned above the apparatus to provide a relatively homogeneous sound field (Tucker-Davis Technologies). Laser stimuli were generated by a pair of calibrated diode lasers, coupled to the animal with flexible, lightweight patch cables. Mice were given at least 5 min to acclimate to the apparatus and cable tethering before each day of training or testing.

Mice were initially shaped to cross between each zone of the chamber in order to terminate a foot shock (0.1–0.5 mA, chosen to be the minimally effective intensity for each mouse). Foot shock terminated after 10 s or upon crossing sides of the avoidance chamber, whichever occurred first. With conditioned crossing behavior established, mice were then trained to associate the target sound (14 kHz, 50 ms tone bursts with 4 ms onset/offset cosine ramps, repetition rate 2.5 Hz, 6 s total duration, 70 dB SPL) with onset of foot shock. Mice learned that they could avoid a foot shock by crossing sides of the chamber before the 6 s stimulus period ended. Crossing during this 6 s period was defined as a hit. Animals were trained with blocks of 10 target trials with randomized inter-trial intervals set to 40 - 50 s.

Once the animal's hit rate exceeded 60% in target-only blocks, the shaping procedure would switch to the foil blocks, where the animal was presented with a train of 8 kHz tone pips that did not predict the onset of shock. Crossing behavior during foil tones was defined as false alarms. No punishment was given on false alarm trials. Similarly, animals were trained with blocks of 10 foil trials with randomized inter-trial intervals between 40 to 50 s. Training continued until the false alarm rate dropped to below 40%, after which the training would switch back to the target blocks. Target and foil shaping blocks would alternate whenever the animal's performance crossed the threshold (higher than 60% hits, lower than 40% false alarms). As the animal reached this stage and its performance d' exceeded 1.0, the animal would be trained with blocks of interleaved target and foil trials (10 targets, 10 foils) until the performance d' plateaued. Once shaping was complete, we determined whether optogenetic activation of L6 CT neurons alone was enough to create a percept that generated a crossing response. This was achieved by delivering laser pulses with the same temporal structure as the auditory stimuli (20 trials consisting of 50 ms pulses with 4 ms onset/offset cosine ramps, repetition rate 2.5 Hz, 6 s duration, 10 mW).

The testing phase consisted of two sets of experiments. The first set of experiments investigated whether L6 CT activation influenced detection thresholds. Four conditions of the laser stimuli were used: three different onset delays (0, 100, and 200 ms for each laser-tone pair) and a control condition with no laser. Target (14 kHz) and foil (8 kHz) frequencies matched the shaping phase but tones were presented across a range of sound levels (0–60 dB SPL in 20 dB steps) and mice were allowed 10 s to cross rather than 6 s. The second set of behavioral experiments investigated L6 CT modulation of tone discrimination performance. These testing blocks used a single tone level (40 dB SPL), but the frequency separation between the target (14 kHz) and foil tone was decreased from 40% (8 kHz) to 20%, 10%, or 5% (foil frequencies: 11.2 kHz, 12.6 kHz, and 13.3 kHz). Foot shock reinforcement was not used during test blocks to avoid learning effects. Trials were randomized across all stimulus conditions (target/foil, sound level, laser delays). Each unique permutation was presented 15 times to generate the complete set of psychometric functions.

For each animal, the discrimination index d' at any stimulus condition was calculated as $z(\text{hit rate}) - z(\text{false alarm rate})$. We fitted every psychometric function with a generalized linear model with a binomially distributed outcome. The threshold for detection or false alarm was derived from the estimated model, and compared across conditions with data from all mice. From the models, sound levels associated with a 50% hit rate were defined as detection thresholds. The target/foil frequency separation associated with a 50% false alarm rate was defined as the discrimination threshold.

Anatomy

Ntsr1-Cre mice were crossed with the Cre-dependent tdTomato reporter line, Ai14 (B6;129S6-Gt(ROSA)26Sor^{tm14(CAG-tdTomato)Hze/J}; stock number 007908). Double-transgenic offspring of either sex aged 6–7 weeks were anesthetized with ketamine (100 mg/kg) and xylazine (10 mg/kg). A surgical plane of anesthesia was maintained throughout the procedure with supplements of ketamine (50 mg/kg) as needed. For both hemispheres, silicon probe recordings were made in MGB using a dorsal approach to identify the location of MGBv using a similar approach described above for unit recordings in head-fixed awake recordings. We then injected 0.3 μl of green retrobeads (LumaFluor Inc.) into the MGBv at 0.05 – 0.1 $\mu\text{l}/\text{min}$ using a motorized injector (Stoelting Co.).

After allowing 7 days for retrograde transport, mice were deeply anesthetized with ketamine and prepared for transcardial perfusion with a 4% formalin solution in 0.1M phosphate buffer. The brains were extracted and post-fixed at room temperature for an additional 12 hr before transfer to 30% sucrose solution. Coronal sections of the brain (40 μm thick) were sectioned with a cryostat. Tissue was immunolabeled for NeuN (rabbit anti-NeuN, abcam) and visualized with Alexafluor 405 (goat anti-rabbit IgG, life tech) to identify neuronal population.

For each injected hemisphere, the MGBv was examined for retrobeads and only cases showing properly positioned injections were included. Two sections from the auditory cortex were selected for quantification. To quantify colocalization of beads in Ntsr1+ neurons, sections were imaged with 3D deconvolution epifluorescence microscopy (Leica) and a 200x200 μm stereotactic plane was established in L6 from the median projection of the stack, with its bottom edge 100 μm above the white matter. Only NeuN+ cells with soma completely contained inside the imaging boundary were further classified for colocalization of markers for Ntsr1 and beads. Cells with NeuN staining as well as the tdTomato fluorescent marker were classified as Ntsr1+ neurons. Cells with at least 3 pixels above threshold in the green channel that were located within the boundary of the NeuN+ somatic compartment were classified as bead+ CT neurons.

QUANTIFICATION AND STATISTICAL ANALYSIS

All statistical analysis was performed with MATLAB (Mathworks). A complete reporting of all statistical tests and outcomes is provided in [Table S1](#). Descriptive statistics are reported as mean \pm SEM unless otherwise indicated. In cases where the same data sample was used for multiple comparisons, we used the Bonferroni correction to adjust for the increased probability of Type-I error. Non-parametric statistical tests were used in select cases where data samples did not meet the assumptions of parametric statistical tests. Statistical significance was defined as $p < 0.05$.

DATA AND SOFTWARE AVAILABILITY

Data acquisition and analysis were performed with custom scripts in MATLAB (Mathworks). Wave_clus, the software package used in this study for spike sorting, can be found at <http://www2.le.ac.uk/departments/engineering/research/bioengineering/neuroengineering-lab/spike-sorting>. Requests for data and custom scripts used in this study can be directed to the lead author (daniel_polley@meei.harvard.edu).

Neuron, Volume 95

Supplemental Information

**A Corticothalamic Circuit for Dynamic Switching
between Feature Detection and Discrimination**

Wei Guo, Amanda R. Clause, Asa Barth-Maron, and Daniel B. Polley

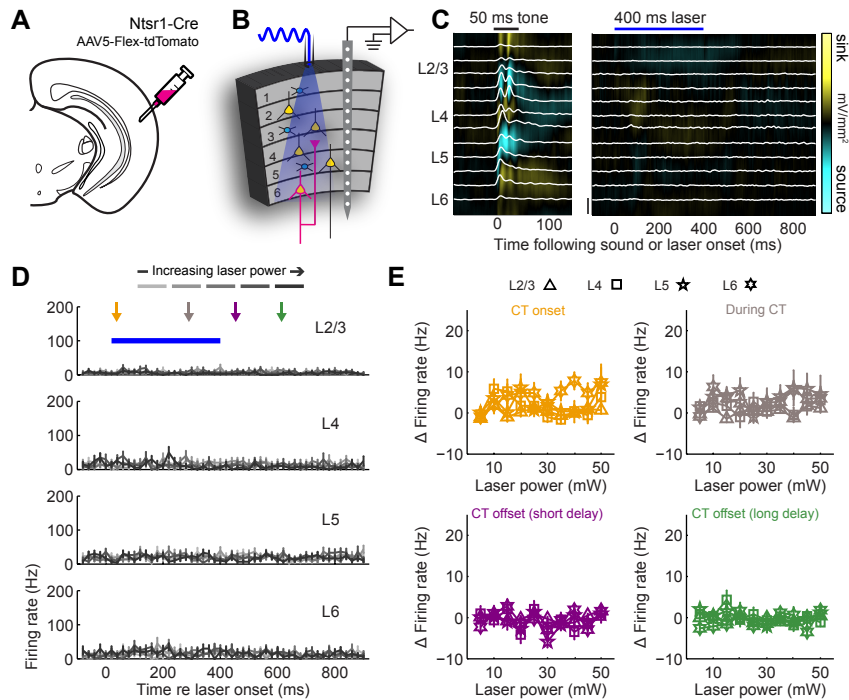


Fig. S1 (related to Figure 2) Laser does not evoke spiking activity from L6CT neurons expressing a control fluorophore. (A) A reporter fluorophore (tdTomato) was expressed in L6 CT neurons by injecting a Cre-dependent viral construct into A1 of Ntsr1-Cre mice. (B) Schematic of columnar recording and laser illumination. (C) Sound-evoked (left) and laser-evoked (right) laminar profiles of current source density (CSD) amplitude from a single A1 penetration in an awake mouse. Multiunit activity (MUA) at each location is represented by the superimposed white peristimulus time histograms (PSTH, scale bar = 100 spikes/s). (D) PSTHs represent the mean MUA in each layer for laser powers ranging from 5-50 mW at the tip of the fiber. Error bars represent 1 SEM. (E) Laser did not evoke spiking activity from any layer (mixed design ANOVA, $F(3) = 0.83$, $p = 0.48$) during any response period (mixed design ANOVA, $F(3) = 0.86$, $p = 0.46$). Error bars represent 1 SEM.

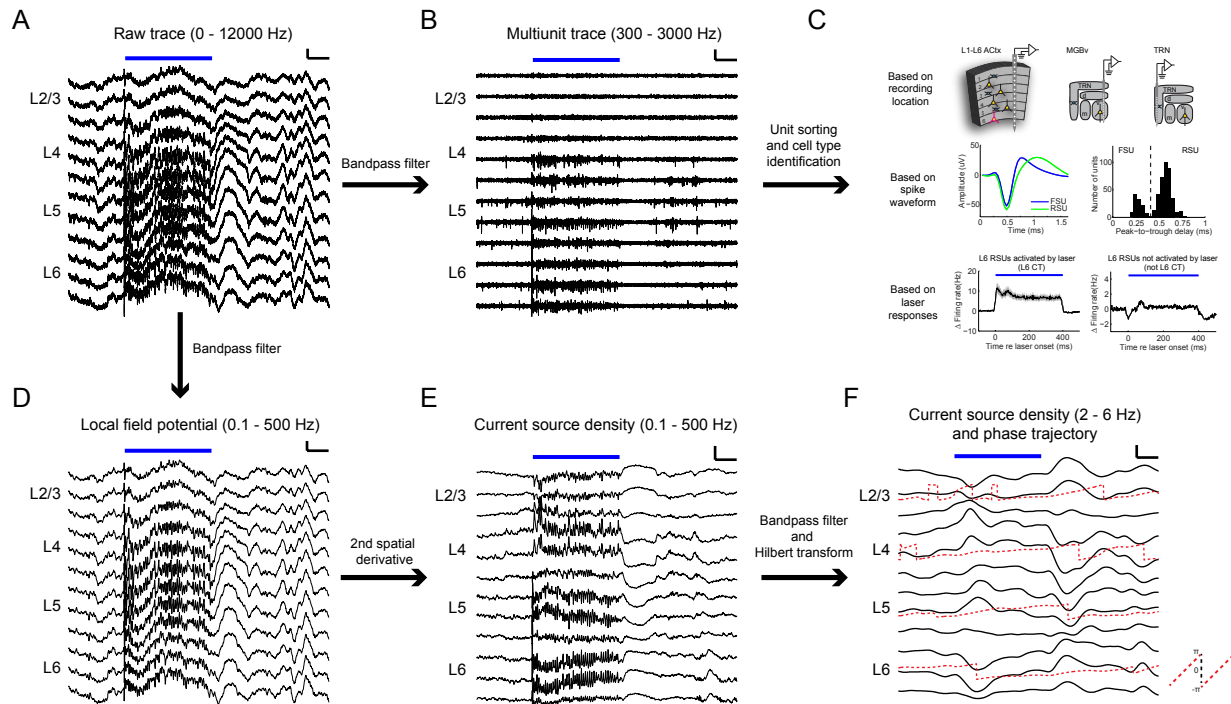


Fig. S2 (related to Figure 6 and 7) Signal processing and analysis of columnar recordings. (A) Unfiltered signal from a 16-channel silicon probe spanning all layers of A1 before, during and after L6 CT activation (scale bars: 100 ms, 250 μ V). (B) The same data, bandpass filtered between 300 – 3000 Hz to reveal multiunit spiking. (scale bars: 100 ms, 100 μ V). (C) Single units waveforms are isolated offline and classified as RS, FS or L6 CT according to waveform shape or sustained response to optogenetic stimulation. Units were classified as fast-spiking units (FSUs, peak-to-trough delay < 0.4 ms) and regular-spiking units (RSUs, peak-to-trough delay > 0.4 ms). Error bars on PSTH represent 1 SEM. (D) Bandpass filtering the raw data in (A) between 0.1 – 500 Hz reveals the local field potential. (scale bars: 100 ms, 250 μ V). (E) The second spatial derivative of the local field potential provides the CSD signal across layers. (scale bars: 100 ms, 5 mV/mm²). (F) CSD traces from (E) can be band-pass filtered between 2-6 Hz and the phase trajectories can be obtained using the Hilbert transform (scale bars: 100 ms, 5 mV/mm²).

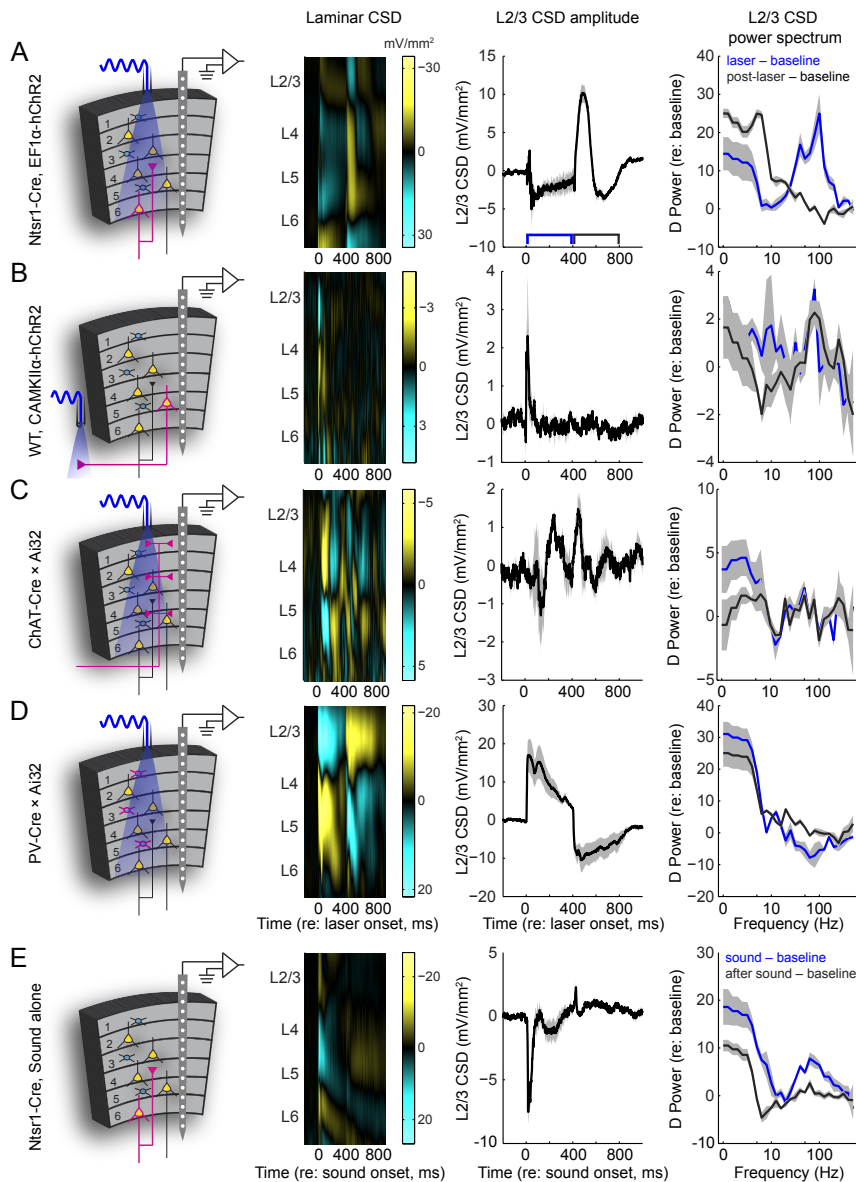


Fig. S3 (related to Figure 6) The laminar pattern of CSD changes evoked by activation of L6 CT neurons is not observed with optogenetic activation of other modulatory cell types. (A-D) Patterns of laser-evoked CSD amplitudes and frequency spectra when ChR2 is expressed in other cell types. First column, cartoon illustrating cell type-specific ChR2 expression. Second column, the laminar pattern of CSD sinks and sources for a representative recording in each condition. Third column, mean (± 1 SEM) L2/3 CSD amplitude. Blue box denotes 400 ms laser period. Black box denotes 400 ms post-laser period. Fourth column, mean (± 1 SEM) change in L2/3 frequency spectrum for the laser and post-laser periods relative to the baseline period (0-400 ms prior to laser onset). (A) L6 CT activation as per Fig. 6. (B) ChR2 is expressed in pyramidal neurons under the CamKIIa promoter. Optogenetic stimulation is restricted to L5 corticofugal neurons by stimulating axon terminals on the dorsal surface of the inferior colliculus, a midbrain structure. (C) Optogenetic activation is limited to cholinergic axons from the basal forebrain by crossing the ChAT-Cre mouse line (B6;129S6-Chatt-m2(cre)Low/J) with the Ai32 mouse line. (D) Optogenetic activation is

limited to parvalbumin-expressing FS interneurons by crossing the PV-Cre mouse line with Ai32 mouse line [Ai32(RCL-ChR2(H134R)/EYFP)], in which ChR2 is expressed in cells with Cre recombinase. (E) Sound-evoked CSD changes in Ntsr1-Cre mice are provided for comparison with optogenetic activation. Note differences in Y-axis scaling between conditions. Also note that the distinctive pattern of high-gamma oscillations during activation followed by a 2-6 Hz large-amplitude post-laser offset CSD signal is only observed with L6 CT activation.

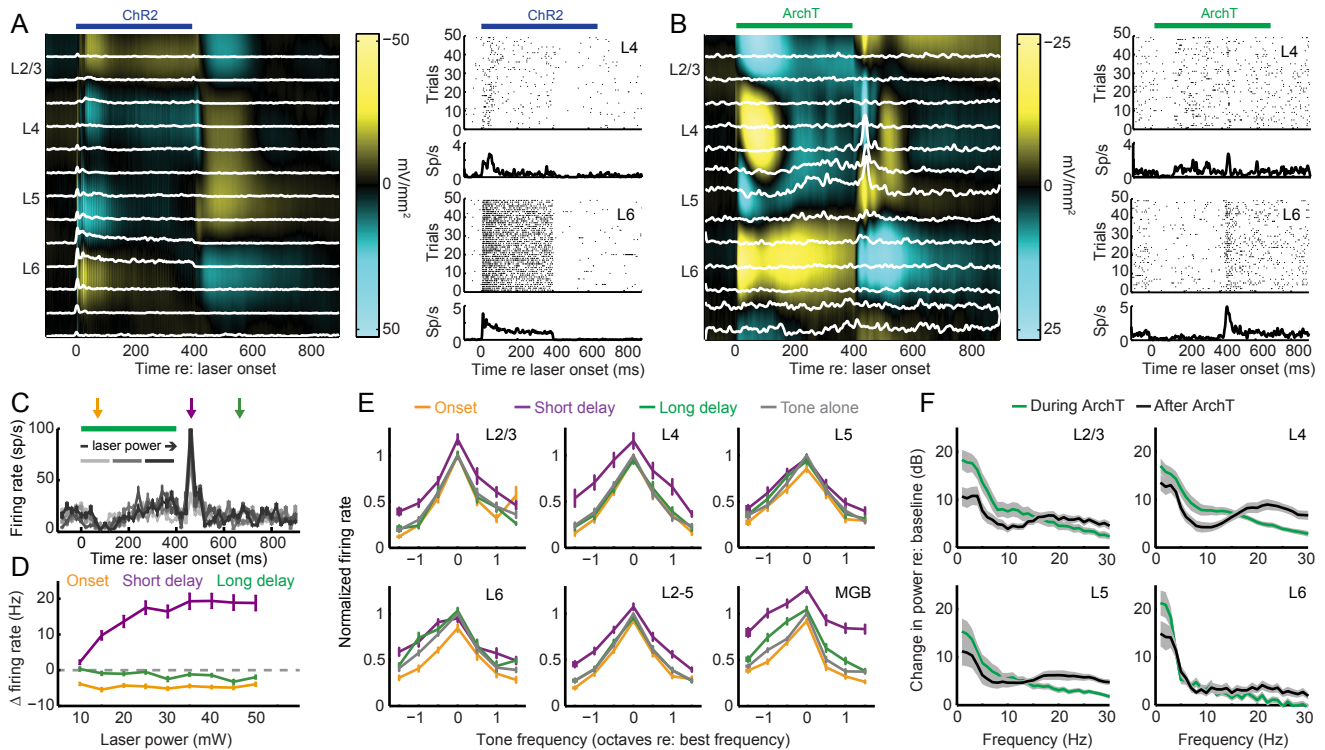


Fig. S4 (related to Figure 2, 5 and 6) Inactivation of L6CT neurons with the hyperpolarizing opsin, ArchT, induces the opposite effects of ChR2 in A1 and MGBv. (A) Left: Columnar CSD pattern in A1 induced by optogenetically activating L6CT neurons with ChR2. Right top: an example L4 unit responding to L6 CT activation. Right bottom: an example L6 CT unit responding to direct photoactivation. (B) Left: Columnar CSD pattern in A1 induced by optogenetically inactivating L6 CT neurons with ArchT. Right top: an example L4 unit firing rate changes before and after L6 CT inactivation. Right bottom: an example of firing rate changes in a L6 unit during inactivation, most likely from a L6 CT unit expressing ArchT. (C) Mean multiunit spiking PSTH from L2-5 relative induced by ArchT activation with laser powers ranging from 5–45 mW (light gray to black, respectively). Orange, purple and green arrows indicate the time epochs used to calculate firing rate changes at the onset, short delay and long delay periods, respectively. (D) Firing rate changes with ArchT inactivation are the opposite of activation with ChR2; relative to the pre-laser spontaneous firing, spiking is suppressed at laser onset, enhanced at a short delay (50 ms) following laser offset and weakly suppressed at a longer delay (150 ms) following laser offset. Dashed gray line indicates no change in firing rate. (E) Normalized tone-evoked firing rate relative to the unit's best frequency for the tone-alone condition (gray line) and the three laser conditions. Responses are enhanced during the short delay period following ArchT inactivation. (F) Changes in the low-frequency power spectrum (0-30 Hz) of the CSD signal for each layer of the A1 column relative to a baseline period for a time window during ArchT inactivation (green line) versus just after laser offset (black line). Error bars for all plots represent 1 SEM.